

# Role of structural relaxations and vibrational excitations in the high-frequency dynamics of liquids and glasses

Song-Ho Chong

*Institute for Molecular Science, Okazaki 444-8585, Japan\**

(Dated: December 24, 2021)

We present theoretical investigation on the high-frequency collective dynamics in liquids and glasses at microscopic length scales and terahertz frequency region based on the mode-coupling theory for ideal liquid-glass transition. We focus on recently investigated issues from inelastic-X-ray-scattering and computer-simulation studies for dynamic structure factors and longitudinal and transversal current spectra: the anomalous dispersion of the high-frequency sound velocity and the nature of the low-frequency excitation called the boson peak. It will be discussed how the sound mode interferes with other low-lying modes present in the system. Thereby, we provide a systematic explanation of the anomalous sound-velocity dispersion in systems – ranging from high temperature liquid down to deep inside the glass state – in terms of the contributions from the structural-relaxation processes and from vibrational excitations called the anomalous-oscillation peak (AOP). A possibility of observing negative dispersion – the *decrease* of the sound velocity upon increase of the wave number – is argued when the sound-velocity dispersion is dominated by the contribution from the vibrational dynamics. We also show that the low-frequency excitation, observable in both of the glass-state longitudinal and transversal current spectra at the same resonance frequency, is the manifestation of the AOP. As a consequence of the presence of the AOP in the transversal current spectra, it is predicted that the transversal sound velocity also exhibits the anomalous dispersion. These results of the theory are demonstrated for a model of the Lennard-Jones system.

PACS numbers: 64.70.Pf, 63.50.+x, 61.20.Lc

## I. INTRODUCTION

The study of high-frequency collective dynamics in liquids and glasses at microscopic length scales and terahertz frequency region has been a subject of intense investigations in the past decade. In particular, recent development of the inelastic X-ray scattering (IXS) technique has renewed the interest in a long-standing issue of sound propagation [1, 2, 3]. It is now generally accepted that a well-defined sound-like oscillatory mode – called the high-frequency or fast sound – is supported in liquids outside the strict hydrodynamic region, down to wavelengths of a few interparticle distances, but with a sound velocity larger than the hydrodynamic value. Traditionally, such increase of the sound velocity upon increase of the wave number – called the anomalous or positive dispersion – has been interpreted within the so-called viscoelastic model [4, 5]. In this model, relevant memory kernel in the Zwanzig-Mori or memory-function equation for the dynamics structure factor  $S_q(\omega)$  is modeled by an exponential function with a single time constant  $\tau$  reflecting structural relaxation in liquids. An increase of the sound velocity is predicted at the wave number  $q$  where the condition  $\omega_q^{\max}\tau = 1$  is fulfilled with the resonance frequency  $\omega_q^{\max}$  of the dynamic structure factor. This condition marks the transition from the low-frequency viscous behavior to the high-frequency elastic behavior of the liquid, and thus, the positive dispersion

effect is ascribed to the transition between a liquid-like to a solid-like response of the system.

According to the viscoelastic model, the absence of the positive dispersion is naturally expected in glasses where the structural relaxation is basically frozen. However, molecular dynamics (MD) simulations have demonstrated the presence of the positive dispersion in model glasses [6, 7, 8, 9, 10]. A first experimental confirmation has been reported recently from an IXS study on vitreous silica [11]. The observed anomalous dispersion implies the presence of some additional “relaxation” process which is active even in glasses, and stimulates an extension of the viscoelastic model to fully account for the anomalies present both in liquids and glasses.

Such extension was also motivated by recent IXS studies on simple liquid metals near the melting temperature [12, 13, 14, 15, 16]. From a detailed line-shape analysis of  $S_q(\omega)$ , the viscoelastic model was found to be unable to account for inelastic peaks in these systems. It was found, instead, that a two-time-scale model for the memory kernel successfully describes the observed spectral shapes. Thus, a convincing experimental demonstration is provided for the simultaneous presence two relaxation processes with slow and fast characteristic time scales, termed structural (labeled  $\alpha$ ) and microscopic (labeled  $\mu$ ) processes. Furthermore, it was pointed out that the faster  $\mu$  process is the major controller of the positive dispersion observed in these systems since it was always found that  $\omega_q^{\max}\tau_\alpha > 1$  for the slower time scale  $\tau_\alpha$ , whereas  $\omega_q^{\max}\tau_\mu$  becomes close to unity at some wave number for the faster time scale  $\tau_\mu$ . According to this experimental observation, the positive dispersion cannot fully be ascribed to the structural relaxation.

---

\*Electronic address: chong@ims.ac.jp

The nature of these two processes have been studied in more detail in Ref. [9] based on the MD simulation for a model of lithium. From the analysis of the simulated  $S_q(\omega)$  with the two-time-scale model, a strong temperature dependence was observed for the time scale  $\tau_\alpha$ , corroborating that the slower process is associated with the structural relaxation. On the other hand, the faster  $\mu$  process was found to persist both in liquid and glass phases with almost no temperature dependence of its relaxation time  $\tau_\mu$ . The persistence of the  $\mu$  relaxation accounts for the presence of the positive dispersion in glasses. Of course, a natural question would be what is relaxing at that low  $T$ , i.e., what is the microscopic nature of the  $\mu$  dynamics. This was studied in Ref. [7] based on the computer simulation for a harmonic glass. There, it was suggested that the origin of this process can be ascribed to the topological disorder, i.e., the decay of the memory kernel is due to the dephasing of different oscillatory components in the force fluctuations.

Besides the peak associated with the high-frequency sound, the MD [8, 10] and IXS [11, 17] works showed the presence of additional low-frequency excitation in the dynamic structure factors  $S_q(\omega)$  or in the related longitudinal current spectra  $\propto \omega^2 S_q(\omega)$ . This second low-frequency excitation – also called the boson peak – exhibits some general characteristics: it appears in the spectra at  $q$  values larger than some fraction of the structure-factor-peak position, and its resonance position is weakly  $q$ -dependent. It was conjectured that the low-frequency excitation reflects the transversal dynamics, and the appearance of the transversal mode in the longitudinal current spectra was interpreted as being due to “mixing” phenomena caused by microscopic disorder [18]. The main evidence supporting this conjecture lies in the simulation results that the low-frequency excitation appears at the same resonance frequency in both of the transversal and longitudinal current spectra, but its intensity is more enhanced in the former. Another support was inferred from studies on the density dependence. The computational work in Ref. [10] demonstrated that the resonance frequency of the low-frequency excitation in the transversal current spectra increases with increasing density. Experimentally, it is observed that upon densification the boson-peak energy shifts to higher energy and its intensity strongly decreases [19, 20, 21, 22]. This parallel of the density dependence was claimed to also suggest that the boson-peak-like low-frequency excitation arises from the transversal dynamics.

In this paper, we present a microscopic and unified explanation of the mentioned features of the high-frequency dynamics in liquids and glasses – the anomalous dispersion of the high-frequency sound velocity and the nature of the low-frequency excitation – which have so far been investigated somewhat independently. This will be done based on the mode-coupling theory (MCT) for ideal liquid-glass transition [23]. Originally, the MCT was developed to deal with structural-relaxation processes which evolve as precursor of the glass transition. On

the other hand, the glass transition also modifies the short-time or the high-frequency dynamics. The study of these modifications was the main subject in Ref. [24]. It was shown there that the strong interaction between density fluctuations at microscopic length scales and the arrested glass structure causes an anomalous-oscillation peak (AOP), which exhibits the properties of the boson peak. As will be demonstrated in the present study, the AOP persists in liquid states as well as in glass states. It will be discussed how the sound mode interferes with other low-lying modes present in the system. Thereby, we provide a systematic explanation of the anomalous sound-velocity dispersion in systems – ranging from high temperature liquid down to deep inside the glass state – in terms of the contributions from the structural-relaxation processes and from the vibrational modes building the AOP. A possibility of observing negative dispersion – the *decrease* of the sound velocity upon increase of the wave number – is argued when the sound-velocity dispersion is dominated by the contribution from the vibrational dynamics. We also show that the low-frequency excitation, observable in both of the glass-state longitudinal and transversal current spectra at the same resonance frequency, is the manifestation of the AOP. This seems to be an alternative interpretation to the mixing phenomena mentioned above. As a natural consequence of the presence of the AOP in the transversal current spectra, it is predicted that the transversal sound velocity also exhibits the anomalous dispersion.

The paper is organized as follows. In Sec. II, the basic MCT equations of motion are formulated, and the model for the demonstration of our theoretical results is specified. Section III deals with the anomalous sound-velocity dispersion of the high-frequency sound, while in Sec. IV we discuss features of glass-state longitudinal and transversal current spectra at low frequencies. Section V concludes the paper.

## II. BASIC THEORY

### A. MCT equations of motion

The basic quantity describing the equilibrium structure of a simple system is the static structure factor  $S_q = \langle |\rho_{\vec{q}}|^2 \rangle$  defined in terms of the density fluctuations for wave vector  $\vec{q}$ ,  $\rho_{\vec{q}} = \sum_{i=1}^N \exp(i\vec{q} \cdot \vec{r}_i) / \sqrt{N}$ . Here,  $N$  is the total number of particles in the system distributed with the average density  $\rho$ , and  $\vec{r}_i$  denotes the position of the  $i$ th particle. For homogeneous and isotropic system, which we assume throughout the paper, the static structure factor depends only on the modulus  $q = |\vec{q}|$ . The most relevant variables characterizing the structural changes as a function of time  $t$  are the density correlators  $\phi_q(t) = \langle \rho_{\vec{q}}(t)^* \rho_{\vec{q}}(0) \rangle / S_q$  which are normalized to unity at  $t = 0$ . The short-time asymptote of these functions is given by  $\phi_q(t) = 1 - (1/2)\Omega_q^2 t^2 + \dots$ , where  $\Omega_q^2$  denotes the square of the characteristic frequency  $\Omega_q^2 = q^2 v^2 / S_q$  [5].

Here  $v = \sqrt{k_B T/M}$  with Boltzmann's constant  $k_B$  denotes the thermal velocity of particle of mass  $M$  at temperature  $T$ . In the small wave-vector limit, one obtains  $\Omega_q = v_0 q + O(q^3)$  with the isothermal sound velocity  $v_0 = v/\sqrt{S_{q=0}}$ . Within the Zwanzig-Mori formalism [5] one can derive the following exact equation of motion

$$\partial_t^2 \phi_q(t) + \Omega_q^2 \phi_q(t) + \Omega_q^2 \int_0^t dt' m_q(t-t') \partial_{t'} \phi_q(t') = 0, \quad (1a)$$

in which the relaxation kernel  $m_q(t)$  is a correlation function of fluctuating forces. Let us introduce Fourier-Laplace transformations to map  $\phi_q$ ,  $m_q$ , and similar functions from the time domain onto the frequency domain according to the convention  $\phi_q(\omega) = i \int_0^\infty dt \exp(i\omega t) \phi_q(t) = \phi_q'(\omega) + i\phi_q''(\omega)$ . Equation (1a) is equivalent to the representation

$$\phi_q(\omega) = -1 / \{ \omega - \Omega_q^2 / [\omega + \Omega_q^2 m_q(\omega)] \}. \quad (1b)$$

Within the MCT, the kernel  $m_q(t)$  is given by a mode-coupling functional of density correlators describing the cage effect of dense systems,

$$m_q(t) = \mathcal{F}_q[\phi(t)]. \quad (2a)$$

Here the mode-coupling functional reads  $\mathcal{F}_q[\tilde{f}] = 1/(2\pi)^3 \int d\vec{k} V(\vec{q}; \vec{k}, \vec{p}) \tilde{f}_k \tilde{f}_p$  with  $\vec{p} = \vec{q} - \vec{k}$ . The coupling coefficients  $V(\vec{q}; \vec{k}, \vec{p})$  are determined by the equilibrium structure. Within the convolution approximation for triple correlations, they are given by  $V(\vec{q}; \vec{k}, \vec{p}) = \rho S_q S_k S_p [\vec{q} \cdot (\vec{k} c_k + \vec{p} c_p)]^2 / (2q^4)$ , where  $c_q$  denotes the direct correlation function related to  $S_q$  via the Ornstein-Zernike equation,  $\rho c_q = 1 - 1/S_q$  [4]. For details, the reader is referred to Ref. [23]. In the following, wave-vector integrals will be approximated by Riemann sums. The mode-coupling functional can then be written as a quadratic polynomial

$$\mathcal{F}_q[\tilde{f}] = \sum_{k,p} V_{q,kp} \tilde{f}_k \tilde{f}_p, \quad (2b)$$

where the indices run over the discretized wave-number grids. The coefficients  $V_{q,kp}$  are trivially related to  $V(\vec{q}; \vec{k}, \vec{p})$ . The  $q \rightarrow 0$  limit of the functional reads

$$\mathcal{F}_0[\tilde{f}] = \sum_k V_k \tilde{f}_k^2, \quad (2c)$$

with  $V_k = (\rho S_0 / 4\pi^2) k^4 S_k^2 [c_k^2 + 2(kc'_k)c_k/3 + (kc'_k)^2/5]$ .

Equations (1) and (2) are closed, provided equilibrium static quantities are known as input. In the following, the results will be demonstrated for the Lennard-Jones (LJ) system: the interaction between two particles is given by the LJ interaction  $V(r) = 4\epsilon_{LJ} \{ (\sigma_{LJ}/r)^{12} - (\sigma_{LJ}/r)^6 \}$ . The first MCT work for the LJ system has been done in Refs. [25, 26] with the optimized random-phase approximation for  $S_q$  [4]. In the present study,  $S_q$  is evaluated

within the Percus-Yevick approximation [4]. Wave numbers will be considered up to a cutoff value  $q^* = 80/\sigma_{LJ}$ , and they are discretized to 400 grid points. From here on, all quantities are expressed in reduced units with the unit of length  $\sigma_{LJ}$ , the unit of energy  $\epsilon_{LJ}$  (setting  $k_B = 1$ ), and the unit of time  $(M\sigma_{LJ}^2/\epsilon_{LJ})^{1/2}$ . The dynamics by varying  $T$  shall be considered for a fixed density  $\rho = 1.093$ , except for Sec. IV B where the dynamics at a lower density  $\rho = 0.95$  is discussed. (We notice that the triple point of the LJ system is at  $\rho^* \approx 0.85$  and  $T^* \approx 0.68$  [27].)

## B. Ideal glass states

The specified model exhibits a fold bifurcation [23]. For small coupling constants  $V_{q,kp}$ , the correlators  $\phi_q(t)$  and the kernels  $m_q(t)$  decay to zero for long times,  $\phi_q(t \rightarrow \infty) = 0$  and  $m_q(t \rightarrow \infty) = 0$ . In this case, the spectra  $\phi_q''(\omega)$  and  $m_q''(\omega)$  are continuous in  $\omega$ . In particular, there hold  $\lim_{\omega \rightarrow 0} \omega \phi_q(\omega) = 0$  and  $\lim_{\omega \rightarrow 0} \omega m_q(\omega) = 0$ . Density fluctuations created at time  $t = 0$  disappear for long times and the same holds for the force fluctuations as expected for an ergodic liquid. For large coupling constants, on the other hand, there is arrest of density fluctuations for long times:  $\phi_q(t \rightarrow \infty) = f_q$ ,  $0 < f_q < 1$ . Thus, nonergodic dynamics is obtained in which the perturbed system does not return to the equilibrium state. Similarly, there is arrest of the force fluctuations,  $m_q(t \rightarrow \infty) = C_q > 0$ . The nonergodicity parameters  $f_q$  and  $C_q$  are connected via [28]

$$f_q = C_q / (1 + C_q), \quad C_q = \mathcal{F}_q[f]. \quad (3)$$

For this strong-coupling solution, the kernel exhibits a zero-frequency pole,  $\lim_{\omega \rightarrow 0} \omega m_q(\omega) = -C_q$ . The fluctuation spectrum  $\phi_q''(\omega) \propto S_q(\omega)$  exhibits a strictly elastic peak:  $\phi_q''(\omega) = \pi f_q \delta(\omega) + \text{regular terms}$ . This is the signature for a solid with  $f_q$  denoting its Debye-Waller factor. Hence, the strong coupling solution deals with a disordered solid; it is a model for an ideal glass state. If one increases the coupling constants smoothly from small to large values, one finds a singular change of the solution from the ergodic liquid to the nonergodic glass state, i.e., an idealized liquid-glass transition. For simple-liquid models, the transition occurs upon cooling at some critical temperature  $T_c$  or upon compression at some critical density  $\rho_c$  [28]. For the LJ model under study where the temperature is considered as a control parameter, one finds  $T_c \approx 1.637$  for  $\rho = 1.093$  within the Percus-Yevick approximation for  $S_q$ . If  $T$  decreases below  $T_c$ ,  $f_q$  increases above its value at the critical point, called the critical nonergodicity parameter or the plateau  $f_q^c$ , as demonstrated in Fig. 1.

## C. MCT liquid-glass-transition dynamics

As precursor of the ideal liquid-glass transition, MCT predicts the evolution of the glassy dynamics which are

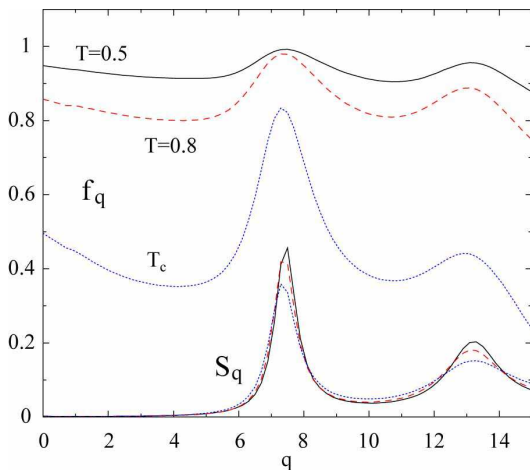


FIG. 1: Debye-Waller factor  $f_q$  and one-tenth of the static structure factor  $S_q$  at  $\rho = 1.093$  for  $T = 0.5$  (solid lines),  $T = 0.8$  (dashed lines), and  $T = T_c \approx 1.637$  (dotted lines).

stretched over many decades. Such MCT scenario has been comprehensively discussed for the hard-sphere system in Refs. [29, 30]. This subsection compiles the MCT universal predictions for the dynamics near the liquid-glass transition to an extent which is necessary for understanding the present article.

We start from introducing some concepts to describe the MCT-liquid-glass-transition dynamics [23]. In the space of control parameters, a smooth function  $\sigma$  is defined near the transition point, called the separation parameter. Glass states are characterized by  $\sigma > 0$ , liquid states by  $\sigma < 0$ , and  $\sigma = 0$  defines the transition point. When only the temperature  $T$  is considered as a control parameter near the transition point, one can write for small distance parameters  $\epsilon = (T_c - T)/T_c$ :  $\sigma = C_T \epsilon$ ,  $C_T > 0$ . In addition, the transition point is characterized by a time scale  $t_0$  and by a number  $\lambda$ ,  $0 < \lambda < 1$ . The scale  $t_0$  specifies properties of the short-time transient dynamics, and  $\lambda$  is called the exponent parameter. The latter determines a certain number  $B > 0$ , the critical exponent  $a$ ,  $0 < a \leq 1/2$ , and the von-Schweidler exponent  $b$ ,  $0 < b \leq 1$ . For the specified LJ model at  $\rho = 1.093$ , we have  $C_T = 0.226$ ,  $\lambda = 0.697$ ,  $a = 0.328$ ,  $b = 0.646$ ,  $B = 0.669$ , and  $t_0 = 0.0125$ .

Let us consider the correlator  $\phi_X(t) = \langle X(t)^* X(0) \rangle$  of some variable  $X$  coupling to the density fluctuations. Its nonergodicity parameter  $f_X = \phi_X(t \rightarrow \infty)$  exhibits a square-root singularity near the transition,

$$f_X = f_X^c + h_X \sqrt{\sigma/(1-\lambda)}, \quad \sigma > 0, \quad \sigma \rightarrow 0. \quad (4)$$

The critical nonergodicity parameter  $f_X^c$  and the critical amplitude  $h_X$  are equilibrium quantities to be calculated from the relevant mode-coupling functionals at the critical point  $T_c$ . At the transition, the correlator exhibits a power-law decay that is specified by the critical exponent  $a$ . In a leading-order expansion in  $(1/t)^a$ , one gets

$$\phi_X(t) = f_X^c + h_X (t_0/t)^a, \quad \sigma = 0, \quad (t/t_0) \rightarrow \infty. \quad (5)$$

For small values of  $\epsilon$ , there is a large time interval, where  $\phi_X(t)$  is close to its critical nonergodicity parameter  $f_X^c$ . Solving the equations of motion asymptotically for this plateau regime, one gets in leading order in the small quantities  $\phi_X(t) - f_X^c$  the factorization theorem:

$$\phi_X(t) = f_X^c + h_X G(t). \quad (6a)$$

The function  $G(t)$ , called the  $\beta$  correlator, is the same for all variables  $X$ , and describes the complete dependence on time and control parameter via the first scaling law

$$G(t) = \sqrt{|\sigma|} g_{\pm}(t/t_{\sigma}), \quad \sigma \gtrless 0. \quad (6b)$$

Here,  $t_{\sigma} = t_0/|\sigma|^{(1/2a)}$  is the first critical time scale. The master functions  $g_{\pm}(\hat{t})$  are determined by  $\lambda$  [31]. For  $\hat{t} \ll 1$ , the master functions are the same on both sides of the transition point, and one gets the power law  $g_{\pm}(\hat{t} \rightarrow 0) = 1/\hat{t}^a$  so that Eq. (5) is reproduced for fixed large  $t$  and  $\sigma$  tending to zero. For  $\hat{t} \gg 1$ , one gets for glasses  $g_+(\hat{t} \gg 1) = 1/\sqrt{1-\lambda}$ , so that Eq. (4) is reproduced. On the other hand, for liquids, one finds for the large rescaled time  $\hat{t}$ :  $g_-(\hat{t} \rightarrow \infty) = -B\hat{t}^b + O(1/\hat{t}^b)$ . Substituting this result into Eqs. (6), one obtains von Schweidler's law for the decay of the liquid correlator below the plateau  $f_X^c$ :

$$\phi_X(t) = f_X^c - h_X (t/t'_{\sigma})^b, \quad t_{\sigma} \ll t, \quad \sigma \rightarrow -0. \quad (7)$$

The control-parameter dependence is given via the second critical time scale  $t'_{\sigma} = t_0 B^{-1/b}/|\sigma|^{\gamma}$  with  $\gamma = (1/2a) + (1/2b)$ . The dynamical process described by the cited results is called the  $\beta$ -process. The  $\beta$  correlator  $G(t)$  describes in leading order the decay of the correlator towards the plateau  $f_X^c$  within the interval  $t_0 \ll t \ll t_{\sigma}$ . For  $t \gg t_{\sigma}$ , the glass correlator arrests at  $f_X$ , while the liquid correlator exhibits von Schweidler's law.

The decay of the liquid correlator below the plateau  $f_X^c$  is called the  $\alpha$ -process. For this process, there holds in leading order for  $\sigma \rightarrow -0$  the second scaling law,  $\phi_X(t) = \tilde{\phi}_X(\tilde{t})$  with  $\tilde{t} = t/t'_{\sigma}$ , which is also referred to as the superposition principle. The control-parameter-independent shape function  $\tilde{\phi}_X(\tilde{t})$  is to be evaluated from the mode-coupling functionals at the critical point. For short rescaled times  $\tilde{t}$ , one gets  $\tilde{\phi}_X(\tilde{t}) = f_X^c - h_X \tilde{t}^b + O(\tilde{t}^{2b})$ , so that Eq. (7) is reproduced. The ranges of applicability of the first and the second scaling laws overlap; both scaling laws yield von Schweidler's law for  $t_{\sigma} \ll t \ll t'_{\sigma}$ .

#### D. Description of the glass-state dynamics

For later convenience, we introduce a reformulation of the MCT equations of motion which is more appropriate in handling the dynamics in glass states [23]. We map the density correlators  $\phi_q$  to new ones  $\hat{\phi}_q$  by

$$\phi_q(t) = f_q + (1 - f_q) \hat{\phi}_q(t). \quad (8a)$$

This amounts to dealing only with the decay relative to the frozen amorphous structure described by  $f_q$ . Introducing new characteristic frequencies  $\hat{\Omega}_q$  by

$$\hat{\Omega}_q^2 = \Omega_q^2 / (1 - f_q), \quad (8b)$$

one obtains for short times  $\hat{\phi}_q(t) = 1 - (1/2)\hat{\Omega}_q^2 t^2 + \dots$  in analogy to the one for  $\phi_q(t)$ . In the small wave-vector limit, there holds  $\hat{\Omega}_q = \hat{v}_0 q + O(q^3)$  with  $\hat{v}_0 = v_0 / \sqrt{1 - f_0}$ . The modification of the sound velocity reflects the reduced compressibility in nonergodic glass states. Substitution of these results into Eq. (1a) reproduces the MCT equations of motion with  $\phi_q$ ,  $\Omega_q$ , and  $m_q$  replaced by  $\hat{\phi}_q$ ,  $\hat{\Omega}_q$ , and  $\hat{m}_q$ , respectively. Here, the new relaxation kernel is related to the original one by

$$m_q(t) = C_q + (1 + C_q) \hat{m}_q(t). \quad (8c)$$

The new correlator has a vanishing long-time limit,  $\lim_{t \rightarrow \infty} \hat{\phi}_q(t) = 0$ , and correspondingly the Fourier-Laplace transform exhibits a regular zero-frequency behavior  $\lim_{\omega \rightarrow 0} \omega \hat{\phi}_q(\omega) = 0$ . Combining Eqs. (3) and (8c), one also concludes that  $\lim_{t \rightarrow \infty} \hat{m}_q(t) = 0$  and  $\lim_{\omega \rightarrow 0} \omega \hat{m}_q(\omega) = 0$ . Since the equation of motion does not change its form, one gets as the analog of Eq. (1b)

$$\hat{\phi}_q(\omega) = -1 / \{ \omega - \hat{\Omega}_q^2 / [\omega + \hat{\Omega}_q^2 \hat{m}_q(\omega)] \}. \quad (8d)$$

The reformulated equation of motion for  $\hat{\phi}_q(t)$  can be closed by finding an expression for the new kernel  $\hat{m}_q(t)$  as a new mode-coupling functional  $\hat{\mathcal{F}}_q$ . One finds combining Eqs. (8a) and (8c) with Eqs. (2a) and (2b) that  $\hat{\mathcal{F}}_q$  is given by a sum of linear and quadratic terms

$$\hat{m}_q(t) = \hat{\mathcal{F}}[\hat{\phi}(t)] = \hat{\mathcal{F}}^{(1)}[\hat{\phi}(t)] + \hat{\mathcal{F}}^{(2)}[\hat{\phi}(t)], \quad (9a)$$

where

$$\hat{\mathcal{F}}_q^{(1)}[\tilde{f}] = \sum_k \hat{V}_{q,k} \tilde{f}_k, \quad \hat{\mathcal{F}}_q^{(2)}[\tilde{f}] = \sum_{k,p} \hat{V}_{q,kp} \tilde{f}_k \tilde{f}_p, \quad (9b)$$

with renormalized coefficients

$$\hat{V}_{q,k} = 2(1 - f_q) \sum_p V_{q,kp} (1 - f_k) f_p, \quad (9c)$$

$$\hat{V}_{q,kp} = (1 - f_q) V_{q,kp} (1 - f_k) (1 - f_p). \quad (9d)$$

Correspondingly, one finds from Eq. (2c) for the zero wave-number limit of the kernel  $m(t) = m_{q=0}(t)$

$$\hat{m}(t) = \hat{m}^{(1)}(t) + \hat{m}^{(2)}(t), \quad (10a)$$

in which linear and quadratic terms are given by

$$\hat{m}^{(1)}(t) = \sum_k \hat{V}_k^{(1)} \hat{\phi}_k(t), \quad \hat{m}^{(2)}(t) = \sum_k \hat{V}_k^{(2)} \hat{\phi}_k(t)^2, \quad (10b)$$

with new coefficients

$$\hat{V}_k^{(1)} = 2(1 - f_0) V_k f_k (1 - f_k), \quad (10c)$$

$$\hat{V}_k^{(2)} = (1 - f_0) V_k (1 - f_k)^2. \quad (10d)$$

As a result, equations of motion are produced, which are of the same form as the original MCT equations (1) and (2). But in addition to the quadratic mode-coupling term, there appears a linear term, and the original mode-coupling coefficients are renormalized to hatted ones. The linear term describes interactions of density fluctuations with the arrested amorphous structure, while the quadratic one deals with two-mode decay processes.

## E. Longitudinal and transversal current correlators

Current correlators are also relevant variables describing the dynamics of dense systems, in particular, when one is interested in vibrational properties. These are defined in terms of the current fluctuations,  $j_{\vec{q}}^\alpha = \sum_{i=1}^N v_i^\alpha \exp(i\vec{q} \cdot \vec{r}_i) / \sqrt{N}$ , where  $\alpha$  ( $= x, y, \text{ or } z$ ) refers to the spatial component and  $v_i^\alpha$  denotes the velocity of the  $i$ th particle. Since  $\langle v_i^\alpha v_j^\beta \rangle = \delta_{ij} \delta_{\alpha\beta} v^2$ , one gets the static correlation  $\langle j_{\vec{q}}^\alpha * j_{\vec{q}}^\beta \rangle = \delta_{\alpha\beta} v^2$ . The current correlators for isotropic system can be represented by two independent functions which depend only on the modulus  $q$ :

$$\langle j_{\vec{q}}^\alpha(t) * j_{\vec{q}}^\beta(0) \rangle / v^2 = \hat{q}^\alpha \hat{q}^\beta \phi_q^L(t) + [\delta_{\alpha\beta} - \hat{q}^\alpha \hat{q}^\beta] \phi_q^T(t). \quad (11)$$

Here  $\hat{q}^\alpha$  denotes the  $\alpha$  component of the unit vector along  $\vec{q}$ . The functions  $\phi_q^L(t)$  and  $\phi_q^T(t)$  are called the longitudinal and transversal current correlators, respectively, and they are normalized to unity at  $t = 0$ .

### 1. Longitudinal current correlator

The density fluctuations and the longitudinal current fluctuations are related via the continuity equation,  $\partial_t \rho_{\vec{q}} = i\vec{q} \cdot \vec{j}_{\vec{q}}$ , and there holds  $\partial_t^2 \phi_q(t) = -\Omega_q^2 \phi_q^L(t)$ . Their Fourier-Laplace transforms therefore satisfy  $\omega[1 + \omega \phi_q(\omega)] = \Omega_q^2 \phi_q^L(\omega)$ , and one obtains from Eq. (1b) for the longitudinal current spectrum  $\phi_q^{L''}(\omega)$

$$\phi_q^{L''}(\omega) = \frac{\omega^2 \Omega_q^2 m_q''(\omega)}{[\omega^2 - \Omega_q^2 \Delta_q(\omega)]^2 + [\omega \Omega_q^2 m_q''(\omega)]^2}, \quad (12)$$

with  $\Delta_q(\omega) = 1 - \omega m_q'(\omega)$ .

The continuity equation holds also in glass states,  $\partial_t^2 \hat{\phi}_q(t) = -\hat{\Omega}_q^2 \hat{\phi}_q^L(t)$  in terms hatted variables defined in Eqs. (8a) and (8b), and their spectra are related via

$$\omega^2 \hat{\phi}_q^{L''}(\omega) = \hat{\Omega}_q^2 \hat{\phi}_q^{L''}(\omega). \quad (13)$$

We therefore have the same expression for  $\phi_q^{L''}(\omega)$  for glass states as in Eq. (12) but with all quantities in the

right-hand side replaced by hatted ones:

$$\phi_q^{L''}(\omega) = \frac{\omega^2 \hat{\Omega}_q^2 \hat{m}_q''(\omega)}{[\omega^2 - \hat{\Omega}_q^2 \hat{\Delta}_q(\omega)]^2 + [\omega \hat{\Omega}_q^2 \hat{m}_q''(\omega)]^2} \quad (\text{glass}), \quad (14)$$

with  $\hat{\Delta}_q = 1 - \omega \hat{m}_q'(\omega)$ . Thus, the same relaxation kernel  $m_q$  or  $\hat{m}_q$  as the one for the density correlator describes the dynamics of the longitudinal current.

## 2. Transversal current correlator

The MCT equations of motion for the transversal current correlator  $\phi_q^T(t)$  have been derived in Ref. [23]. The Zwanzig-Mori equation is given by

$$\phi_q^T(t) + (\Omega_q^T)^2 \int_0^t dt' m_q^T(t-t') \phi_q^T(t') = 0, \quad (15a)$$

and its Fourier-Laplace transform reads

$$\phi_q^T(\omega) = -\frac{1}{\omega + (\Omega_q^T)^2 m_q^T(\omega)}, \quad (15b)$$

with  $(\Omega_q^T)^2 = q^2 v^2$ . The relaxation kernel  $m_q^T(t)$  is a correlation function of transversal fluctuating forces. Within the MCT, the transversal fluctuating forces are approximated by their projection onto the subspace spanned by the density products, and with the factorization approximation the kernel is given by a mode-coupling functional  $\mathcal{F}_q^T$  of the density correlators

$$m_q^T(t) = \mathcal{F}_q^T[\phi(t)], \quad \mathcal{F}_q^T[f] = \sum_{k,p} V_{q,kp}^T \tilde{f}_k \tilde{f}_p. \quad (16a)$$

Here  $V_{q,kp}^T = \rho S_k S_p [\vec{e}^T \cdot (\vec{k}c_k + \vec{p}c_p)]^2 / (2q^2)$  with  $\vec{e}^T$  denoting a unit vector orthogonal to  $\vec{q}$ . The  $q \rightarrow 0$  limit of the functional is given by

$$\mathcal{F}_0^T[f] = \sum_k V_k^T \tilde{f}_k^2, \quad (16b)$$

with  $V_k^T = (\rho/60\pi^2)k^4 [c'_k S_k]^2$ . These MCT equations of motion for  $\phi_q^T(t)$  can be solved with the knowledge of the static quantities and of the density correlators.

In glass states,  $m_q^T(\omega)$  acquires a zero-frequency pole since the transversal force fluctuations do not decay to zero for long times,  $m_q^T(t \rightarrow \infty) = C_q^T > 0$ . We therefore write in analogy to Eq. (8c)

$$m_q^T(t) = C_q + C_q^T \hat{m}_q^T(t), \quad C_q^T = \mathcal{F}_q^T[f], \quad (17)$$

and introduce  $\hat{m}_q^T(t)$  for the description of the glass-state transversal current dynamics. The new kernel satisfies  $\lim_{t \rightarrow \infty} \hat{m}_q^T(t) = 0$  and  $\lim_{\omega \rightarrow 0} \omega \hat{m}_q^T(\omega) = 0$ . Substituting the Fourier-Laplace transform of Eq. (17) into Eq. (15b) yields for the transversal current spectrum

$$\phi_q^{T''}(\omega) = \frac{\omega^2 (\hat{\Omega}_q^T)^2 \hat{m}_q^{T''}(\omega)}{[\omega^2 - (\hat{\Omega}_q^T)^2 \hat{\Delta}_q^T(\omega)]^2 + [\omega (\hat{\Omega}_q^T)^2 \hat{m}_q^{T''}(\omega)]^2}, \quad (18)$$

where  $\hat{\Omega}_q^T = \Omega_q^T \sqrt{C_q^T}$  and  $\hat{\Delta}_q^T = 1 - \omega \hat{m}_q^{T'}(\omega)$ .

The reformulated equation of motion for the glass-state transversal current dynamics can be closed by finding an expression for  $\hat{m}_q^T(t)$  as a new mode-coupling functional  $\hat{\mathcal{F}}_q^T$ . One finds from Eqs. (8a), (16a), and (17) that  $\hat{\mathcal{F}}_q^T = \hat{\mathcal{F}}_q^{T(1)} + \hat{\mathcal{F}}_q^{T(2)}$  in analogy to Eq. (9a). Correspondingly, there holds  $\hat{m}_T(t) = \hat{m}_T^{(1)}(t) + \hat{m}_T^{(2)}(t)$  for  $\hat{m}_T(t) = \hat{m}_{q=0}^T(t)$ . Explicit expressions for the new mode-coupling functionals shall be omitted here for brevity: they take the same form as in Eqs. (9) and (10), but with coupling coefficients replaced by the ones for the transversal current correlators.

The mathematical form of Eq. (18) for glass states is identical to that for the longitudinal current given in Eq. (14). In particular,  $\phi_q^{T''}(\omega)$  for glass states vanishes proportional to  $\omega^2$  for small frequencies in contrast to the one in liquid states. Thus, the transversal current correlators exhibit a drastic difference between liquid and glass states [23]: the long wave length correlators in liquids describe diffusive processes, while the ones in the glass states describe the propagation of transversal sound waves as expected for an isotropic elastic continuum.

## 3. Velocity correlator

Finally, we briefly summarize here for later discussion the MCT equations of motion for the normalized velocity correlator  $\Psi(t) = \langle \vec{v}_s(t) \cdot \vec{v}_s(0) \rangle / (3v^2)$  defined with the velocity  $\vec{v}_s$  of a tagged particle (labeled  $s$ ). An exact equation for this quantity is given by

$$\partial_t \Psi(t) + v^2 \int_0^t dt' m_s(t-t') \Psi(t') = 0, \quad (19)$$

and the MCT expression for the kernel  $m_s(t)$  reads

$$m_s(t) = \sum_k V_k^s \phi_k^s(t) \phi_k(t), \quad (20)$$

with  $V_k^s = (\rho/6\pi^2)k^4 c_k^2 S_k$  [23, 32]. Here  $\phi_q^s(t) = \langle \rho_q^s(t) \rho_q^s(0) \rangle$  with  $\rho_q^s = \exp(i\vec{q} \cdot \vec{r}_s)$  denotes tagged-particle density correlator. The Zwanzig-Mori equation for  $\phi_q^s(t)$  has the same form as Eq. (1a) with  $\phi_q$ ,  $m_q$ , and  $\Omega_q^2$  replaced by  $\phi_q^s$ ,  $m_q^s$ , and  $(\Omega_q^s)^2 = q^2 v^2$ , respectively, and the MCT kernel is given by the functional  $m_q^s(t) = \sum_{k,p} V_{q,kp}^s \phi_k^s(t) \phi_p(t)$  with  $V_{q,kp}^s$  determined by  $S_q$  [28, 30]. For glass states, the MCT equations for  $\Psi(t)$  can be reformulated in terms of the hatted kernel  $\hat{m}_s(t)$  defined in analogy to Eq. (17) via

$$m_s(t) = C_s + C_s \hat{m}_s(t), \quad C_s = \lim_{t \rightarrow \infty} m_s(t). \quad (21)$$

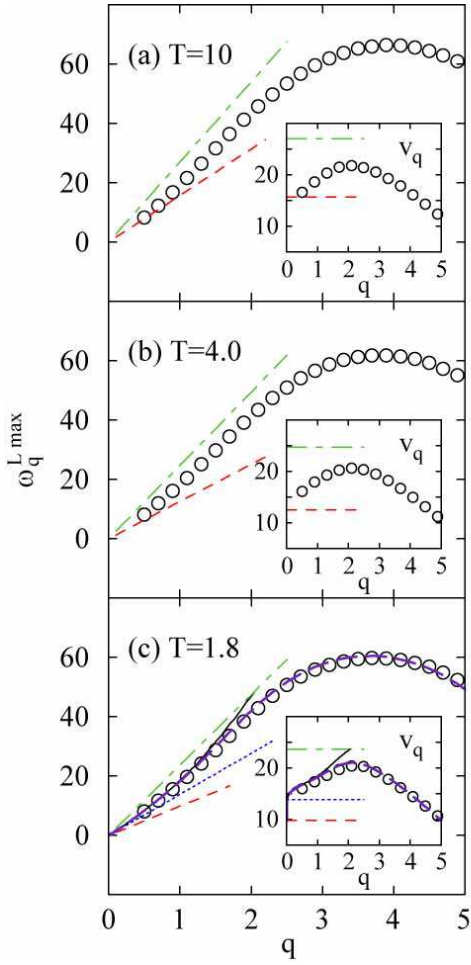


FIG. 2: Peak positions  $\omega_q^{L,\max}$  (circles) of the longitudinal current spectra  $\phi_q^{L''}(\omega)$  as a function of  $q$  at  $\rho = 1.093$  for temperatures indicated in each panel referring to liquid states. Dashed lines denote the hydrodynamic dispersion law  $qv_0$  with the isothermal sound velocity  $v_0$ . Dash-dotted lines show the linear dispersion law  $qv_\infty$  with the infinite-frequency sound velocity  $v_\infty$ . The insets exhibit apparent sound velocities  $v_q = \omega_q^{L,\max}/q$  (circles) as a function of  $q$  along with horizontal lines denoting  $v_0$  (dashed lines) and  $v_\infty$  (dash-dotted lines). Dotted lines in (c) refer to the linear dispersion law  $qv_\infty^\alpha$  and the velocity  $v_\infty^\alpha$  discussed in the text (*cf.* Sec. III D). Long-dashed lines through circles in (c) are from the solution to Eq. (23), while solid lines are based on Eqs. (24).

### III. ANOMALOUS DISPERSION OF SOUND-VELOCITY

#### A. Dispersion relation

Circles in Fig. 2 show the dispersion relation – the peak positions  $\omega_q^{L,\max}$  of the longitudinal current spectra  $\phi_q^{L''}(\omega)$  as a function of wave number  $q$  – for three representative temperatures referring to liquid states. (We notice that, in experimental and computer-simulation studies for the dispersion relation cited in Sec. I, it is the

peak positions of the longitudinal current spectra that are usually reported. The peak positions of the dynamic structure factors  $\propto \phi_q''(\omega)$  and of the longitudinal current spectra  $\phi_q^{L''}(\omega)$  nearly coincide as can be inferred, e.g., from Fig. 12. In the present article, we are primarily interested in the wave-number regime  $q \lesssim 4$  where  $\omega_q^{L,\max}$  increases with  $q$ . In this pseudo first Brillouin zone, the peaks  $\omega_q^{L,\max}$  are associated with the collective mode.) The dashed line in each panel denotes the hydrodynamic dispersion law  $qv_0$  with the isothermal sound velocity  $v_0$  [33], whereas the dash-dotted line exhibits the linear dispersion law  $qv_\infty$  defined in terms of the infinite-frequency sound velocity  $v_\infty$  (see below). The inset in each panel shows an apparent sound velocity  $v_q = \omega_q^{L,\max}/q$  (circles) as a function of  $q$ , along with horizontal lines denoting  $v_0$  (dashed line) and  $v_\infty$  (dash-dotted line). The increase of the sound velocity  $v_q$  from  $v_0$  towards  $v_\infty$  upon increase of the wave number  $q$ , which is observable for  $q \lesssim 2$  in all the insets of Fig. 2, is called the anomalous or positive dispersion.

There are subtle variations in the anomalies depending on the temperature. At high temperature  $T = 10$ , the whole increase of the sound velocity is observable in Fig. 2(a) starting from  $v_0$  at small  $q$  up to close to  $v_\infty$  at  $q \approx 2$ . This feature is altered if the temperature is decreased. For  $T = 4.0$  (Fig. 2(b)), the sound velocity  $v_q$  for small wave numbers is still located above the hydrodynamic value  $v_0$ . For  $T = 1.8$  (Fig. 2(c)), this “gap” becomes larger, and the sound velocity  $v_q$  in the small- $q$  limit seems to approach another limit denoted by the dotted line which will be defined below.

Corresponding results for representative glass states are shown in Fig. 3. But here, the hydrodynamic dispersion law  $q\hat{v}_0$  is determined by  $\hat{v}_0$  introduced in connection with Eq. (8b) (see also below). It is clear from Fig. 3 that the anomalous sound-velocity dispersion is present also in glass states. Again, there are subtle variations in the appearance of the anomalies. For  $T = 1.47$  (Fig. 3(b)), the sound velocity  $v_q$  approaches the hydrodynamic value  $\hat{v}_0$  rather rapidly for  $q \rightarrow 0$ . On the other hand, for  $T = T_c$  (Fig. 3(a)), the approach towards  $\hat{v}_0$  is retarded. For the deep-in-glass state  $T = 0.5$  (Fig. 3(c)), a new feature shows up, and “negative” dispersion is observable for  $q < 1$ , where the sound velocity  $v_q$  is smaller than the hydrodynamic value  $\hat{v}_0$ .

The results shown in Figs. 2(b), 2(c), and 3(a) indicate that the increase of the sound velocity from the hydrodynamic value has already started at smaller wave-number regime which cannot be adequately resolved with the linear  $q$  axis. In addition, the presence of the negative dispersion shown in Fig. 3(c) implies that the anomalous sound-velocity dispersion cannot be accounted for solely in terms of relaxation processes since those processes would lead only to the positive dispersion as known, e.g., from the viscoelastic model.

In the following, a microscopic and unified understanding of the mentioned anomalies shall be attempted. This will be done based on the generalized hydrodynamic de-

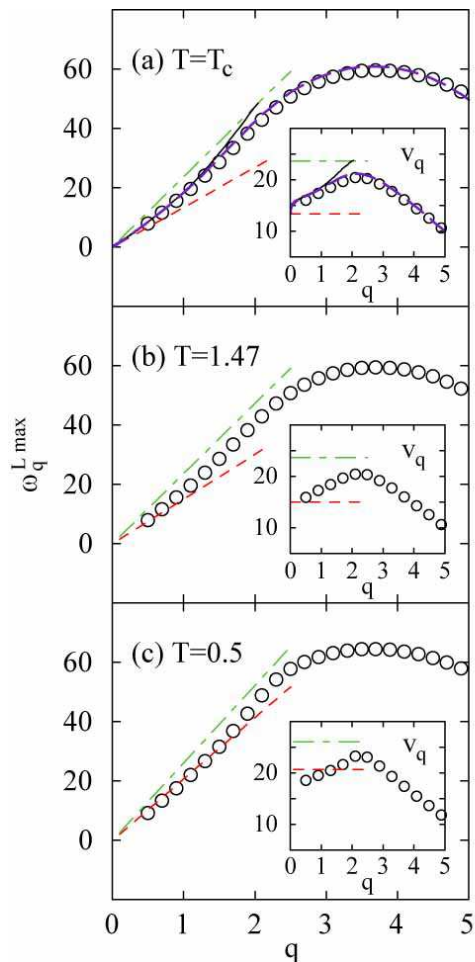


FIG. 3: The same as in Fig. 2, but here temperatures refer to glass states, and the hydrodynamic dispersion law  $q\hat{v}_0$  is determined by  $\hat{v}_0$  defined in the text. Long-dashed lines through circles in (a) are from the solution to Eq. (23), while solid lines are based on Eqs. (24).

scription [24]. In this description, the memory kernel  $m_q(\omega)$  is approximated by its  $q \rightarrow 0$  limit, while the full  $\omega$  dependence of  $m(\omega) = m_{q=0}(\omega)$  is retained. In this manner, one gets from Eq. (12) [34]

$$\phi_q^{L''}(\omega) \approx \frac{\omega^2 \Omega_q^2 m''(\omega)}{[\omega^2 - \Omega_q^2 \Delta(\omega)]^2 + [\omega \Omega_q^2 m''(\omega)]^2}, \quad (22)$$

with  $\Delta(\omega) = 1 - \omega m'(\omega)$ . In lowest order, the resonance frequency  $\omega_q^{L, \max}$  can be obtained as a solution to

$$\omega_q^{L, \max} = \Omega_q \sqrt{\Delta(\omega = \omega_q^{L, \max})}. \quad (23)$$

The long-dashed lines through circles in Figs. 2(c) and 3(a) show the dispersion law and the sound velocity based on the solution to this equation. One understands that the lowest-order solution describes the results from the full MCT solutions (circles) fairly well for the whole  $q$ -range shown in the figure. Since we are interested in the

small wave-number region  $q \lesssim 2$  where the anomalous sound-velocity dispersion is present, a further simplification is possible: one can replace  $\Omega_q$  by its leading-order contribution,  $\Omega_q \approx qv_0$ . This yields

$$\omega_q^{L, \max} = qv_0 \sqrt{\Delta(\omega = \omega_q^{L, \max})}, \quad (24a)$$

which can be rewritten for the the sound velocity  $v_q$  as

$$v_q = v_0 \sqrt{\Delta(\omega = qv_q)}. \quad (24b)$$

The solid lines in Figs. 2(c) and 3(a) exhibit the dispersion law and the sound velocity based on the solutions to these equations. One understands that no serious error is introduced with the use of Eqs. (24) as far as the regime  $q \lesssim 2$  of interest is concerned.

Before proceeding, let us show that Eqs. (24) reproduce known results [4, 5] in the limit of small and large resonance frequencies. The hydrodynamic sound is obtained by taking the  $\omega \rightarrow 0$  limit of  $\Delta(\omega)$  in Eqs. (24). One obtains the dispersion law  $\omega_q^{L, \max} = qv_0 \sqrt{1 + m(t \rightarrow \infty)}$  since  $\lim_{\omega \rightarrow 0} \omega m'(\omega) = -\lim_{t \rightarrow \infty} m(t)$ . For liquids where the memory kernel relaxes to zero for long times,  $m(t \rightarrow \infty) = 0$ , the dispersion law  $\omega_q^{L, \max} = qv_0$  is obtained with the isothermal sound velocity  $v_0$  [33]. For glasses, on the other hand, the kernel does not decay to zero for long times,  $m(t \rightarrow \infty) = C$ , leading to the dispersion law  $\omega_q^{L, \max} = q\hat{v}_0$  with  $\hat{v}_0 = v_0 \sqrt{1 + C}$ . (This agrees with  $\hat{v}_0 = v_0 / \sqrt{1 - f_0}$  given below Eq. (8b) because of Eq. (3).) These results have been included with dashed lines in Figs. 2 and 3. In the high-frequency limit, one obtains, using  $\lim_{\omega \rightarrow \infty} \Delta(\omega) = 1 + \lim_{t \rightarrow 0} m(t)$ , the dispersion law  $\omega_q^{L, \max} = qv_\infty$  with the infinite-frequency sound velocity  $v_\infty = v_0 \sqrt{1 + m(t=0)}$ . This holds for both liquid and glass states, and has been included with dash-dotted lines in Figs. 2 and 3.

Thus, on the basis of Eq. (24b), it is clear that the anomalous sound-velocity dispersion from the low-frequency hydrodynamic value ( $v_0$  for liquids and  $\hat{v}_0$  for glasses) towards the infinite-frequency one  $v_\infty$  upon increase of the wave number  $q$  is controlled by the detailed frequency dependence of  $\Delta(\omega)$ . This in turn is determined by the relaxation of the memory kernel  $m(t)$ . Within the MCT,  $m(t)$  is given in terms of the mode-coupling functional as  $m(t) = \mathcal{F}_0[\phi(t)]$  [cf. Eq. (2c)]. In the following two subsections, the details of the relaxation of  $m(t)$  and of the frequency dependence of  $\Delta(\omega)$  will be investigated. These results will be employed in Sec. III D for a systematic study of the anomalies.

## B. Structural-relaxation processes

Figure 4 exhibits the evolution of the dynamics of  $m(t)$  upon decrease of the temperature  $T$ . The curve for  $T = 10$ , which is quite higher than  $T_c \approx 1.637$ , decays rapidly and nearly exponentially to zero. By lowering the

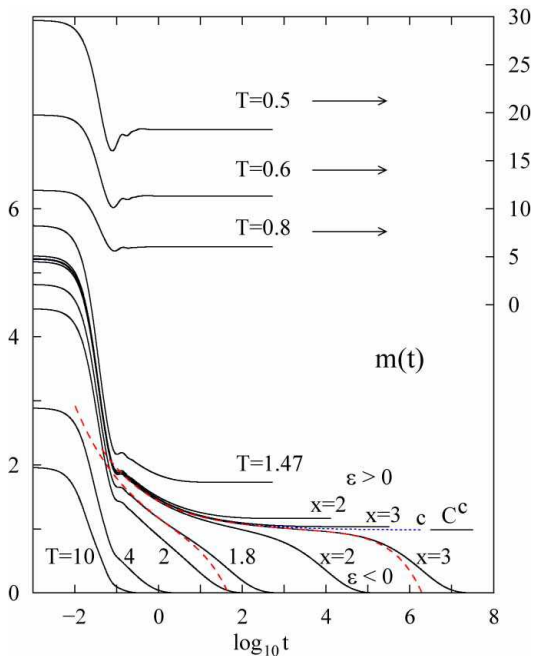


FIG. 4: The memory kernel at  $q = 0$ ,  $m(t) = m_{q=0}(t)$ , as a function of  $\log_{10} t$  at  $\rho = 1.093$  for temperatures indicated in the figure. Curves with labels  $x = 2$  and  $3$  are calculated for distance parameters  $\epsilon = (T_c - T)/T_c = \mp 10^{-x}$  for liquids ( $\epsilon < 0$ ) and for glasses ( $\epsilon > 0$ ). Dotted line with label  $c$  denotes the kernel at  $T_c$ . Horizontal line marks the plateau height  $C^c$ . Dashed lines show the MCT asymptotic-law results based on Eq. (25) for  $T = 1.8$  and  $x = 3$  ( $\epsilon < 0$ ). The kernels for  $T = 0.5, 0.6$ , and  $0.8$  refer to the right vertical axis.

temperature, the dynamics becomes slower and stretched due to the development of the cage effect. For temperatures close to but above  $T_c$ , the kernel  $m(t)$  exhibits a two-step relaxation: the dynamics towards the plateau  $C^c$ , followed by the final relaxation from the plateau to zero. The dynamics that occurs near the plateau is referred to as the  $\beta$  process, whereas the final relaxation is called the  $\alpha$  process (*cf.* Sec. II C). The  $\beta$  process for small  $|T - T_c|$  can be well described by the MCT asymptotic formula (6a) specialized to  $m(t)$

$$m(t) = C^c + DG(t), \quad (25)$$

as exemplified with the dashed lines in Fig. 4. ( $C^c = 0.982$  and  $D = 1.925$  for the model under study.) At the critical point  $T_c$ , the kernel approaches the plateau in a stretched manner, as shown by the dotted curve with label  $c$  in Fig. 4. This process, called the critical decay, is described by a power law [*cf.* Eq. (5)]

$$m(t) = C^c + D(t_0/t)^a. \quad (26)$$

Decreasing  $T$  below the critical temperature  $T_c$ , the values for the long-time limits  $C$  increase. These limits are approached exponentially fast for  $T \neq T_c$  [35]. If  $T$  is far below  $T_c$ , one observes enhanced oscillatory features for times near  $\log_{10} t \approx -1.2$  as can be seen from the curves

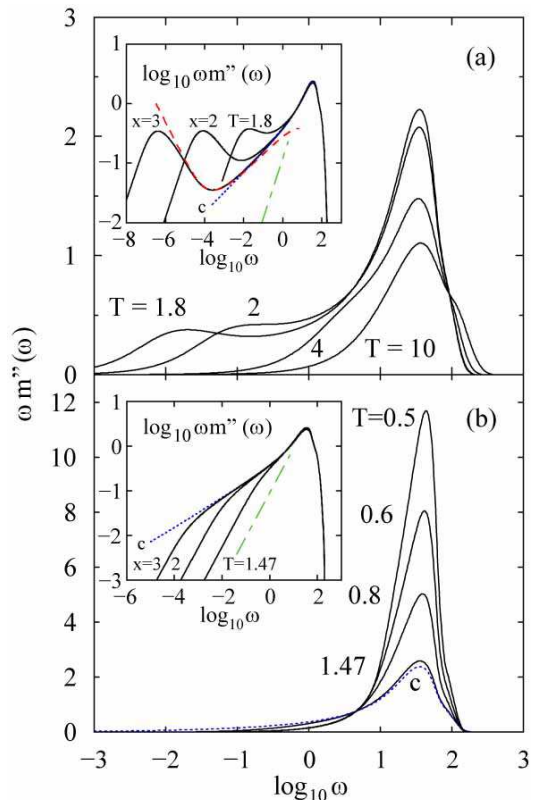


FIG. 5: Susceptibility spectra  $\omega m''(\omega)$  for the memory kernels  $m(t)$  shown in Fig. 4 for liquid states (a) and for glass states (b). The insets exhibit the double logarithmic representation of the spectra for  $T$  close to  $T_c$ . The meaning of the labels  $x = 2$  and  $x = 3$  is the same as in Fig. 4. Dotted line with label  $c$  denotes the susceptibility spectrum at  $T_c$ . Dashed line in the upper inset shows the MCT asymptotic-law result based on Eq. (27) for  $x = 3$  ( $\epsilon < 0$ ). Dash-dotted lines in the insets exhibit the hydrodynamic linear law  $\sim \omega$ .

for  $T = 0.8, 0.6$ , and  $0.5$  in Fig. 4. Such vibrational dynamics reflects the anomalous-oscillation peak (AOP) discussed in Ref. [24]. It is caused by strong interaction between density fluctuations at microscopic length scales and the arrested glass structure. Features of the AOP will be discussed in the next subsection.

Figure 5 shows the susceptibility spectra  $\omega m''(\omega)$  of the kernels shown in Fig. 4. The spectrum at  $T = 10$  exhibits only one peak located at high frequencies, to be called a microscopic peak. By lowering  $T$ , an additional peak emerges at low frequencies reflecting the evolution of the structural-relaxation processes. The lower frequency peak, whose position decreases strongly by lowering  $T$ , is due to the  $\alpha$  process, and is called the  $\alpha$  peak. It is separated from the microscopic peak by a minimum, called the  $\beta$  minimum. The appearance of the minimum is caused by the crossover from a power law  $\sim t^{-a}$  to another one  $\sim -t^b$  which occurs in the  $\beta$  regime (*cf.* Sec. II C). For small  $|T - T_c|$ , the  $\beta$  minimum is well

described by the formula which follows from Eq. (25),

$$\omega m''(\omega) = D\omega G''(\omega), \quad (27)$$

as exhibited by the dashed line in the inset of Fig. 5(a). At  $T = T_c$ , the critical decay (26) leads to a sublinear susceptibility variation

$$\omega m''(\omega) = D \sin(\pi a/2) \Gamma(1-a) (\omega t_0)^a, \quad (28)$$

as shown by the dotted line with label *c*. Here,  $\Gamma(x)$  denotes the Gamma function. Below  $T_c$ , the final exponential decay towards  $C$  [35] implies the hydrodynamic law in the small- $\omega$  limit,  $\omega m''(\omega \rightarrow 0) \propto \omega$ . But, near  $T_c$ , there is a frequency interval where the spectrum is described by the sublinear critical spectrum (28). This produces a “knee” at some frequency where the crossover from the linear low-frequency spectrum  $\omega m''(\omega) \propto \omega$  to the sublinear critical one  $\omega m''(\omega) \propto \omega^a$  occurs, as can be inferred from the inset of Fig. 5(b). If  $T$  is far below  $T_c$ , the knee disappears, and the spectrum is dominated by a single peak reflecting the AOP (see the next subsection). This holds for  $T = 0.8, 0.6$ , and  $0.5$ . It is interesting to notice that there is only a weak temperature dependence in the position  $\log_{10} \omega \approx 1.5$  of the high-frequency peak from high- $T$  liquids down to deep-in-glass states. This feature will also be studied in the next subsection.

Figure 6 shows the reactive part of the normalized longitudinal moduli  $\Delta(\omega) = 1 - \omega m'(\omega)$ . Since  $m'(\omega)$  and  $m''(\omega)$  are related via the Kramers-Kronig relation [4], features for  $\Delta(\omega)$  can be understood from those for the susceptibility spectra just mentioned. In particular, a peak in  $\omega m''(\omega)$  implies a strong increase of  $\Delta(\omega)$  near that peak frequency. This way, one understands an almost single-step increase of  $\Delta(\omega)$  at  $\log_{10} \omega \approx 1.5$  for  $T \gg T_c$  and  $T \ll T_c$ , reflecting the presence of only the high-frequency microscopic peak in  $\omega m''(\omega)$  for those temperatures (*cf.* Fig. 5). For  $T \gtrsim T_c$ , on the other hand, the presence of two peaks in  $\omega m''(\omega)$  explains the two-step increase of  $\Delta(\omega)$  shown in Fig. 6(a). Because of the strong  $T$  dependence of the  $\alpha$ -peak frequency, the position where the low- $\omega$  variation of  $\Delta(\omega)$  occurs depends strongly on the temperature. In addition, the sublinear susceptibility variation  $\omega m''(\omega) \propto \omega^a$ , present both in liquid and glass states near  $T_c$ , also leads to the enhancement of  $\Delta(\omega)$ . Indeed, it follows from Eq. (26) that

$$\Delta(\omega) = 1 + C^c + D \cos(\pi a/2) \Gamma(1-a) (\omega t_0)^a, \quad (29)$$

holds near the  $\beta$  minimum for liquids or near the knee position for glasses. The curve based on this formula (dashed line) is compared with the memory kernel at the critical point (dotted line) in the inset of Fig. 6(b).

For later convenience, let us define the  $\alpha$  and  $\beta$  regimes for  $\Delta(\omega)$ . We start from liquid states. Since the memory kernel  $m(t)$  decays from the plateau  $C^c$  to zero in the  $\alpha$  regime, corresponding  $\alpha$  regime for  $\Delta(\omega)$  shall be defined as the frequency interval  $0 < \omega < \omega_\alpha^+$  in which  $\omega_\alpha^+$  satisfies  $\Delta(\omega_\alpha^+) = 1 + C^c$ . Thus, the  $\alpha$  regime for  $\Delta(\omega)$  is below the horizontal bar marking  $1 + C^c$  in Fig. 6(a).

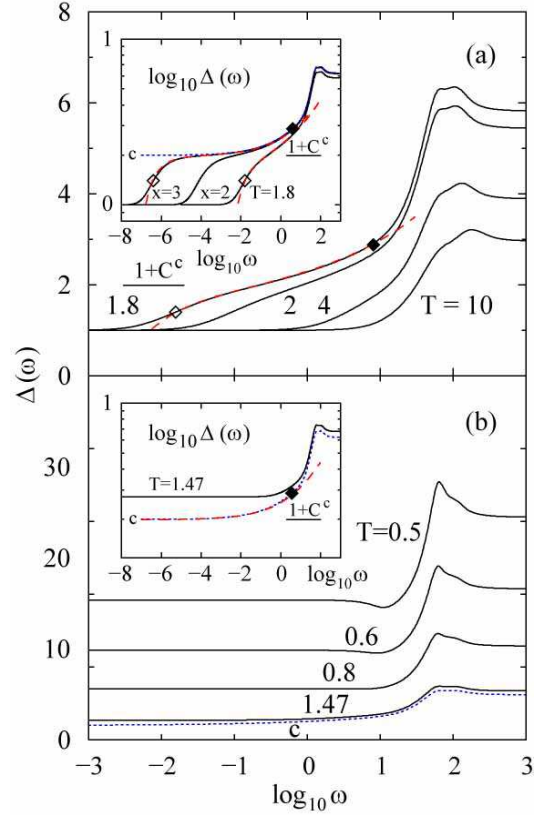


FIG. 6: Reactive part of the normalized longitudinal moduli  $\Delta(\omega) = 1 - \omega m'(\omega)$  for the memory kernels  $m(t)$  shown in Fig. 4 for liquid states (a) and for glass states (b). The insets exhibit the double logarithmic representation of  $\Delta(\omega)$  for  $T$  close to  $T_c$ . The meaning of the labels  $x = 2$  and  $x = 3$  is the same as in Fig. 4. Dotted line with label *c* denotes  $\Delta(\omega)$  at  $T_c$ . Horizontal lines mark the plateau height  $1 + C^c$  (see text). Dashed lines in the upper inset show the MCT asymptotic-law results based on Eq. (30) for  $T = 1.8$  and  $x = 3$  ( $\epsilon < 0$ ), while dashed line in the lower inset exhibits the curve based on Eq. (29). The open ( $\omega_\beta^-$ ) and filled ( $\omega_\beta^+$ ) diamonds refer to the frequencies  $\omega_\beta^\pm$  defined in the text.

In the  $\beta$  regime, the kernel  $m(t)$  is well described by the MCT asymptotic formula (25) (*cf.* Fig. 4). The corresponding  $\beta$  regime shall be defined as the one where  $\Delta(\omega)$  can be well described by the asymptotic formula

$$\Delta(\omega) = 1 + C^c - D\omega G'(\omega), \quad (30)$$

which follows from Eq. (25). The dashed lines in Fig. 6(a) show curves based on this formula. Let us introduce  $\omega_\beta^\pm$  as the frequencies where  $\Delta(\omega)$  (solid lines) differ from the MCT asymptotic formula (30) (dashed lines) by 2%. These frequencies are marked by open ( $\omega_\beta^-$ ) and filled ( $\omega_\beta^+$ ) diamonds in Fig. 6(a), and the frequency interval  $\omega_\beta^- < \omega < \omega_\beta^+$  shall be considered as the  $\beta$  regime for  $\Delta(\omega)$ . As mentioned in Sec. II C, there is an overlap between the  $\alpha$  and  $\beta$  regimes. For glass states, the  $\beta$  regime for  $\Delta(\omega)$  shall be defined as the frequency interval  $\omega < \omega_\beta^+$  where  $\omega_\beta^+$  marks the point at which  $\Delta(\omega)$

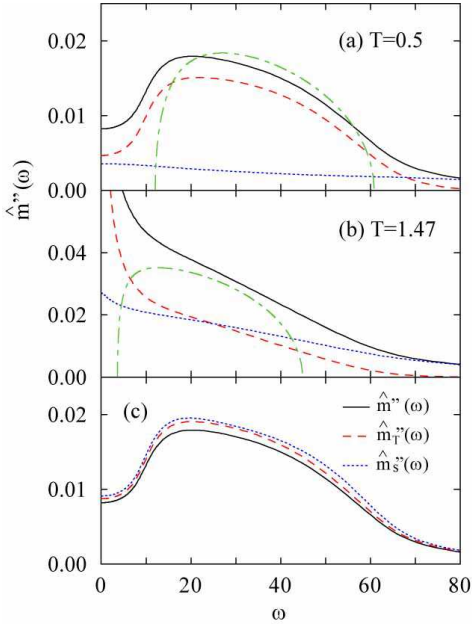


FIG. 7: (a) Solid line denotes the memory-kernel spectrum  $\hat{m}''(\omega)$  for  $\rho = 1.093$  and  $T = 0.5$ , and dashed and dotted lines respectively refer to its one-mode and two-mode contributions,  $\hat{m}^{(1)''}(\omega)$  and  $\hat{m}^{(2)''}(\omega)$ . Dash-dotted line shows the SGA spectrum  $\hat{m}_{\text{SGA}}''(\omega)$  based on Eqs. (31). (b) The same as in (a), but for  $T = 1.47$ . (c) Comparison of the memory-kernel spectrum  $\hat{m}''(\omega)$  (solid line) with  $\hat{m}_T''(\omega)$  (dashed line) for the transversal current correlator and  $\hat{m}_s''(\omega)$  (dotted line) for the velocity correlator for  $\rho = 1.093$  and  $T = 0.5$ .

differs from the MCT asymptotic formula (29) by 2%. The frequency  $\omega_\beta^+$  at the critical point is marked by the filled diamond in the inset of Fig. 6(b).

### C. Vibrational excitations

In contrast to the structural-relaxation processes, there is only a weak temperature dependence in the time scale for the short-time dynamics in  $m(t)$  occurring at  $\log_{10} t \lesssim -1$  (cf. Fig. 4). Correspondingly, the high-frequency peaks in the susceptibility spectra  $\omega m''(\omega)$  are located nearly at the same frequencies  $\log_{10} \omega \approx 1.5$  from high- $T$  liquid down to deep-in-glass state (cf. Fig. 5), leading to a common increase of  $\Delta(\omega)$  around this frequency regime (cf. Fig. 6). In this section, nature of such high-frequency microscopic process shall be discussed.

We start from temperatures far below  $T_c$ ,  $T \ll T_c$ , called stiff-glass states, which are characterized by the Debye-Waller factors close to unity as exemplified by the curve for  $T = 0.5$  shown in Fig. 1. One understands from Eqs. (9c) (9d), (10c), and (10d) that the renormalized coupling coefficients become very small for the stiff-glass states, and they decrease towards zero in the limit  $\eta = 1 - f_q \rightarrow 0$ . Furthermore, the two-mode contributions to the kernels get suppressed relative to the one-mode

contributions, in particular  $\hat{m}^{(2)}(t)/\hat{m}^{(1)}(t) = O(\eta)$ . Figure 7(a) shows the hatted spectrum  $\hat{m}''(\omega)$  for  $T = 0.5$  (solid line) along with its one-mode  $\hat{m}^{(1)''}(\omega)$  (dashed line) and two-mode  $\hat{m}^{(2)''}(\omega)$  (dotted line) contributions (cf. Eq. (10a)). It is seen that the one-mode contribution  $\hat{m}^{(1)''}(\omega)$  indeed provides the dominant contribution to the total memory-kernel spectrum  $\hat{m}''(\omega)$ . The role played by the two contributions  $\hat{m}^{(1)}$  and  $\hat{m}^{(2)}$  is utterly different. The former describes the AOP, while the latter provides a background spectrum.

Further properties of the AOP have been discussed in Ref. [24] based on a stiff-glass approximation (SGA), which is obtained by dropping the two-mode contributions to the memory kernels. (See also Ref. [36] on the SGA.) In particular, it has been found that harmonic oscillations of the particles within their cages are a good description of the relevant modes, and the density correlator as well as the memory kernel in the stiff-glass states can be described as a superposition of independent harmonic oscillator spectra where the distribution of oscillator frequencies is caused by the distribution of sizes and shapes of the cages. According to the cited MCT result for the AOP, one obtains  $\hat{m}(\omega) \approx \hat{m}_{\text{SGA}}(\omega)$  with

$$\omega \hat{m}_{\text{SGA}}(\omega) = w_1 [\tilde{\chi}(\omega) - 1]. \quad (31a)$$

Here  $\tilde{\chi}(\omega)$  is given by a superposition of undamped harmonic-oscillator spectra

$$\tilde{\chi}(\omega) = \int_{\omega_-^2}^{\omega_+^2} d\xi \tilde{\rho}(\xi) \chi_\xi(\omega), \quad (31b)$$

$$\tilde{\rho}(\xi) = \sqrt{(\omega_+^2 - \xi)(\xi - \omega_-^2)} / (2\pi w_1), \quad (31c)$$

$$\chi_\xi(\omega) = -\tilde{\Omega}^2 / [\omega^2 - \tilde{\Omega}^2 \xi + i\omega\nu]. \quad (31d)$$

The weight distribution  $\tilde{\rho}(\xi)$  for the oscillators with frequency  $\sqrt{\xi}\tilde{\Omega}$  extends from the low-frequency threshold  $\Omega_- = \omega_- \tilde{\Omega}$  to the high-frequency one  $\Omega_+ = \omega_+ \tilde{\Omega}$ , where  $\omega_\pm = 1 \pm \sqrt{w_1}$  with an integrated coupling coefficient  $w_1 = \sum_k \hat{V}_k^{(1)}$  (cf. Eq. (10c)).  $\tilde{\Omega}$  denotes some average value of  $\hat{\Omega}_q$  defined in Eq. (8b) over the  $q$  range  $q \gtrsim q_D$  [24]. Here,  $q_D = (6\pi^2 \rho)^{1/3}$  denotes the Debye wave number, and  $q_D = 4.02$  for the density  $\rho = 1.093$ . Since the  $q$  range around the first peak position  $q_{\text{max}}$  of the static structure factor  $S_q$  is known to constitute the dominant contribution to the kernel [28],  $\tilde{\Omega}$  in the present study is taken as an average of the first maximum and first minimum of  $\hat{\Omega}_q$ , which occurs at  $q \approx q_D$  and  $q_{\text{max}}$ , respectively (cf. Fig. 13). A friction term  $\nu$  is necessary when one wants to incorporate the neglected two-mode contributions in a perturbative manner [24], but one may read the formulas with  $\nu = 0$  unless stated otherwise. Figure 7(a) demonstrates that Eqs. (31) with  $\nu = 0$  (dash-dotted line) describe qualitative features of the AOP of  $\hat{m}''(\omega)$  for  $T = 0.50$ .

By increasing  $T$ , one observes enhanced intensity in  $\hat{m}''(\omega)$  at low frequencies as shown for  $T = 1.47$  in

Fig. 7(b). This is a precursor phenomenon of the glass melting at the transition point. Near  $T_c$ , such enhancement for decreasing frequencies can be described by a critical power law  $\sim \omega^{a-1}$  (*cf.* Eq. (28)). By substituting the critical decay of the density correlators  $\hat{\phi}_q(t) \sim t^{-a}$  into Eq. (10b), one understands that it is the linear term  $\hat{m}^{(1)}(t)$  that provides the critical decay of  $\hat{m}(t)$ , whereas the quadratic term  $\hat{m}^{(2)}(t)$  serves only as a correction  $O(t^{-2a})$ . This explains why in Fig. 7(b) the strong increase of the intensity is dominated by  $\hat{m}^{(1)''}(\omega)$  (dashed line). Thus, the modes building the AOP are buried under the tail of the central peak, and they show up only as a shoulder. Nevertheless, it is remarkable that the SGA spectrum  $\hat{m}''_{\text{SGA}}(\omega)$  (dash-dotted line) succeeds to extract the buried AOP portion as demonstrated in Fig. 7(b). The shift of the AOP to lower frequencies upon increase of the temperature reflects the widened size of the cages so that particles “bounce” in their cages with smaller average frequencies. Indeed, the particles are localized in such tight cages at  $T = 0.5$  that the square root  $\delta r = \sqrt{\langle \delta r^2(t \rightarrow \infty) \rangle}$  of the long-time limit of the mean-squared displacement [30] is only 5.0% of the particle’s LJ diameter, whereas it is increased to  $\delta r = 0.139$  at  $T = 1.47$ . The shift is accompanied by an increase of the inelastic spectrum including the AOP, reflecting the decrease of the elastic contribution  $\pi C \delta(\omega)$ .

The analysis presented in Fig. 7(b) also implies a possibility to extract AOP portion in the spectrum on the basis of Eqs. (31). So, let us examine to what extent the high-frequency microscopic peaks in the susceptibility spectra  $\omega m''(\omega)$  at higher temperatures have such “harmonic” character. This is done in Fig. 8 where representative susceptibility spectra taken from Fig. 5 are compared with the SGA susceptibility spectra

$$\omega m''_{\text{SGA}}(\omega) = (1 + C) w_1 \tilde{\chi}''(\omega), \quad (32)$$

which follows from Eqs. (8c) and (31a). To focus on the high-frequency regime, the comparison is done in Fig. 8 with the linear- $\omega$  axis. In evaluating the SGA susceptibility spectra for liquids, nonergodicity parameters  $f_q$  and  $C$  in the equations and quantities involved are replaced by the ones at the critical point.

As discussed in connection with Figs. 7(a) and 7(b), the SGA spectra describe the AOP portion of the memory-kernel spectra for  $T = 0.5$  and  $T = 1.47$  fairly well, and this is reflected in the susceptibility spectra shown in the two bottom panels of Fig. 8. Somewhat large deviation seen at  $\omega \gtrsim 40$  for  $T = 1.47$  is due to the neglected two-mode contribution, which is more enhanced than the deviation in Fig. 7(b) due to the presence of the factor  $\omega$  in  $\omega m''(\omega)$ . On the other hand, because of this factor, the deviation at small frequencies seen in Fig. 7(b) is suppressed for  $\omega m''(\omega)$ .

One understands from the other panels of Fig. 8 that the harmonic approximation based on Eq. (32) reasonably accounts for overall features – peak position and strength – of the microscopic peaks in  $\omega m''(\omega)$  not only near  $T_c$  but even at high temperatures such as  $T = 10$ .

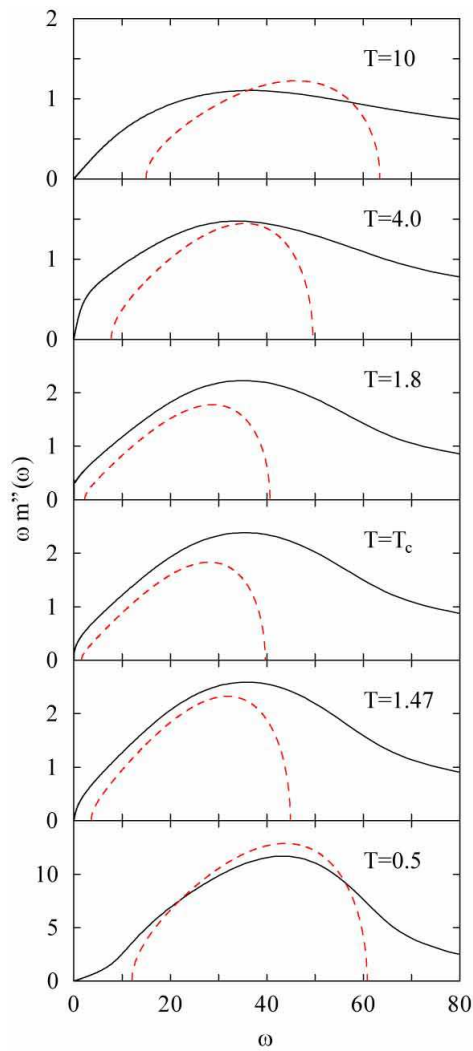


FIG. 8: Susceptibility spectra  $\omega m''(\omega)$  (solid lines) at indicated temperatures taken from Fig. 5, but plotted here on the linear- $\omega$  axis. Dashed lines denote the SGA susceptibility spectra  $\omega m''_{\text{SGA}}(\omega)$  based on Eq. (32).

The large deviations for low frequencies at  $T = 4.0$  and  $10$  simply reflect the fact that at such high  $T$  the structural-relaxation contributions also enter into the high-frequency regime (*cf.* Fig. 5). Thus, considerable portion of the short-time or high-frequency microscopic process, from high- $T$  liquids down to deep-in-glass states, can be described as a superposition of harmonic vibrational dynamics. This explains the weak  $T$  dependence of the microscopic process shown in Figs. 4-6.

The persistence of the vibrational dynamics inside the cage in the liquid state is not surprising. To see this, we show in Fig. 9 the velocity correlator  $\Psi(t)$  for representative liquid and glass states. It is well known that the cage effect in dense liquids manifests itself by oscillatory variations with a decay of  $\Psi(t)$  to negative values [4], and Fig. 9(a) demonstrates this phenomenon. That such oscillatory dynamics exhibited by  $\Psi(t)$  reflects the AOP

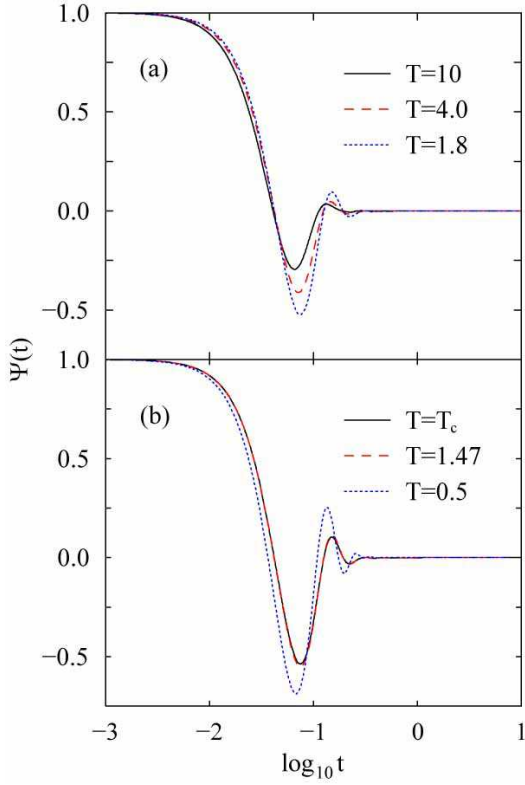


FIG. 9: Normalized velocity correlator  $\Psi(t)$  at  $\rho = 1.093$  for temperatures referring to liquid states (a) and glass states (b).

can be understood from the observations (i) in the stiff-glass state  $T = 0.5$  the spectrum  $\hat{m}''_s(\omega)$  of the relaxation kernel for  $\Psi(t)$  exhibits an AOP whose spectral features – threshold frequencies and maximum position and height – nearly coincide with those for the AOP of  $\hat{m}''(\omega)$  as demonstrated in Fig. 7(c), and (ii) at higher  $T$  including liquid states there is a correlation between the peak position in the SGA susceptibility spectra  $\omega m''_{\text{SGA}}(\omega)$  shown in Fig. 8 and the time at which the velocity correlator  $\Psi(t)$  reaches the first minimum.

There is another interesting feature caused by the dominant harmonic nature of the dynamics in stiff-glass states. From  $\Delta(\omega)$  for  $T = 0.5$  shown in Fig. 6(b), one observes the decrease of  $\Delta(\omega)$  from  $\Delta(\omega = 0) = 1 + C$  at  $\log_{10} \omega \approx 1$ . One can show that such behavior is also well described by the harmonic approximation: it follows from Eqs. (8c) and (31a) that the reactive part of the modulus within the SGA is given by

$$\Delta_{\text{SGA}}(\omega) = (1 + C) \{ 1 - w_1 [\tilde{\chi}'(\omega) - 1] \}. \quad (33)$$

Figure 10 compares  $\Delta(\omega)$  for  $T = 0.5$  with the curve based on Eq. (33) on the linear- $\omega$  axis. One understands that decrease of  $\Delta(\omega)$  from  $\Delta(\omega = 0) = 1 + C$  observable at  $\omega \approx 10$  is due to the harmonic modes near the threshold frequency  $\Omega_-$ . Similarly, the bump at  $\omega \approx 60$  reflects the harmonic modes near  $\Omega_+$ .

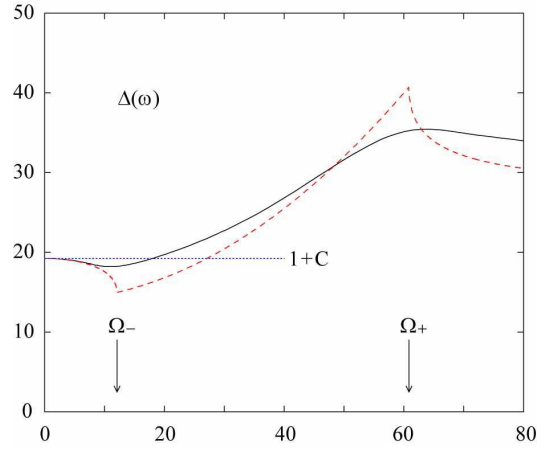


FIG. 10: Reactive part of the longitudinal modulus  $\Delta(\omega)$  (solid line) for  $\rho = 1.093$  and  $T = 0.5$  taken from Fig. 6, but plotted here on the linear- $\omega$  axis. Dashed line exhibits the SGA modulus  $\Delta_{\text{SGA}}(\omega)$  based on Eq. (33). Horizontal dotted line denotes  $\Delta(\omega = 0) = 1 + C$ . Vertical arrows mark the threshold frequencies  $\Omega_-$  and  $\Omega_+$  defined in the text.

#### D. Structural-relaxation and vibrational-dynamics contributions to sound-velocity dispersion

Here we provide an explanation of the anomalous sound-velocity dispersion shown in Figs. 2 and 3 based on Eq. (24b) and on the features of  $\Delta(\omega)$  explored in the previous two subsections.

At  $T = 10$ , the whole relaxation of the memory kernel  $m(t)$  occurs on the short time scale  $\log_{10} t \lesssim -1$  (Fig. 4). This yields a susceptibility spectrum  $\omega m''(\omega)$  consisting only of the microscopic peak located at  $\log_{10} \omega \approx 1.5$  (Fig. 5), and the entire increase of  $\Delta(\omega)$  occurs in the frequency regime  $\log_{10} \omega > 0$  (Fig. 6). It is therefore sufficient to use the linear- $\omega$  axis to describe the whole  $\omega$  variation in  $\Delta(\omega)$ , and this explains via Eq. (24b) the observation in Fig. 2(a) that the entire positive dispersion of the sound velocity  $v_q$  starting from  $v_0$  up to close to  $v_\infty$  occurs within the linear- $q$  axis.

By decreasing the temperature to  $T = 4.0$ , the relaxation of  $m(t)$  becomes slower and stretched due to the development of the cage effect (Fig. 4), leading to the evolution of low-frequency contributions in  $\omega m''(\omega)$  and  $\Delta(\omega)$  (Figs. 5 and 6). Translated to  $v_q$  via Eq. (24b), this means that the approach of  $v_q$  towards the hydrodynamic value  $v_0$  becomes delayed compared to the one at  $T = 10$ . This explains why  $v_q$  for small wave numbers shown in Fig. 2(b) is still located above  $v_0$ .

For temperatures close to but above  $T_c$ , the memory kernel  $m(t)$  exhibits the glassy structural relaxations (Fig. 4), leading to low- $\omega$  variations in  $\omega m''(\omega)$  and  $\Delta(\omega)$  which can be adequately described only with the  $\log_{10} \omega$  axis (Figs. 5 and 6). Let us analyze the sound-velocity increase for  $T = 1.8$  in detail. For this purpose, we replot the inset of Fig. 2(c) in Fig. 11(a), but with the  $\log_{10} q$  axis. This is necessary to fully appreciate the small- $q$

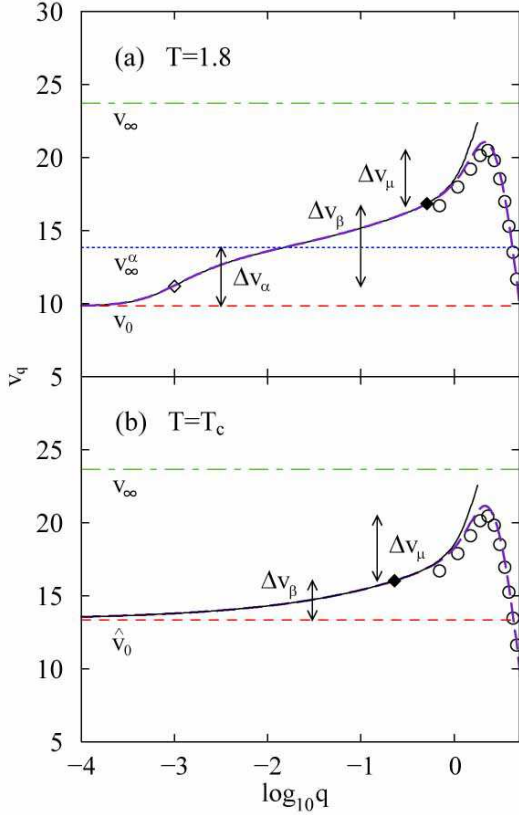


FIG. 11: (a) Apparent sound velocity  $v_q = \omega_q^{L\max}/q$  (circles) for  $\rho = 1.093$  and  $T = 1.8$ , taken from the inset of Fig. 2(c), but plotted here with the  $\log_{10} q$  axis. Long-dashed line is from the solution to Eq. (23), while solid line is based on Eq. (24b). Horizontal lines denote  $v_0$  (dashed line),  $v_\infty$  (dash-dotted line), and  $v_\infty^\alpha$  (dotted line). The contributions  $\Delta v_\alpha$ ,  $\Delta v_\beta$ , and  $\Delta v_\mu$  to the sound-velocity increase defined in the text are indicated by vertical arrows. The open and filled diamonds respectively mark  $v_\beta^-$  and  $v_\beta^+$  defined in the text. (b) The same as in (a), but here the sound velocity refers to  $T = T_c$ , taken from the inset of Fig. 3(a), and horizontal dashed line denotes  $\hat{v}_0 = v_0\sqrt{1+C}$ .

variation of the sound velocity  $v_q$ , which on the basis of Eq. (24b) originates from the glassy low- $\omega$  variations in  $\Delta(\omega)$ . Notice that the circles from the full MCT solutions for  $\phi_q^{L''}(\omega)$  can be obtained only up to the minimum value of the discretized wave-number grids. On the other hand, there is no such restriction in the solution (solid line) to the lowest-order equation (24b) of the generalized hydrodynamic description. The difference between the circles and the solid line – in the  $q$  range where the circles are available – is due to the approximations involved, but there should be no problem to use the approximate solution for understanding the essence of the anomalies.

Let us quantify the contributions to the sound velocity increase due to the  $\alpha$  process (to be denoted as  $\Delta v_\alpha$ ), due to the  $\beta$  process ( $\Delta v_\beta$ ), and due to the microscopic process ( $\Delta v_\mu$ ) in the following way based on the  $\alpha$  and  $\beta$  regimes for  $\Delta(\omega)$  defined at the end of Sec. III B. As

mentioned there,  $\Delta(\omega)$  varies from  $\Delta(\omega = 0) = 1$  to  $\Delta(\omega_\alpha^+) = 1 + C^c$  in the  $\alpha$  regime. One therefore obtains from Eq. (24b):  $\Delta v_\alpha = v_\infty^\alpha - v_0$  with  $v_\infty^\alpha = v_0\sqrt{1+C^c}$ . The notation comes from the fact that  $v_\infty^\alpha$  is the high-frequency limit of the sound velocity in the  $\alpha$  regime. The horizontal dotted line in Fig. 11(a) marks  $v_\infty^\alpha$ , and corresponding linear dispersion law  $qv_\infty^\alpha$  and the velocity  $v_\infty^\alpha$  have been included with dotted lines in Fig. 2(c). The  $\beta$ -relaxation contribution  $\Delta v_\beta$  can be obtained in terms of the frequencies  $\omega_\beta^\pm$  also introduced at the end of Sec. III B: one obtains from Eq. (24b)  $\Delta v_\beta = v_\beta^+ - v_\beta^-$  with  $v_\beta^\pm = v_0\sqrt{\Delta(\omega_\beta^\pm)}$ . These velocities are marked by open ( $v_\beta^-$ ) and filled ( $v_\beta^+$ ) diamonds in Fig. 11(a). The rest of the sound-velocity increase towards  $v_\infty$  is due to the microscopic process. As mentioned in the previous subsection, considerable portion of the microscopic process is due to the harmonic vibrational dynamics. The contributions  $\Delta v_\alpha$ ,  $\Delta v_\beta$ , and  $\Delta v_\mu$  are indicated by vertical arrows in Fig. 11(a). Since there is an overlap between the  $\alpha$  and  $\beta$  regimes (*cf.* Sec. II C), there is a corresponding overlap between  $\Delta v_\alpha$  and  $\Delta v_\beta$ .

The full sound-velocity variation for  $T = 1.8$  can be understood in this way in terms of the contributions from  $\alpha$ - and  $\beta$ -relaxation processes and from the microscopic vibrational dynamics. Notice that the structural-relaxation contributions can be adequately described only with the logarithmic  $q$  axis. This explains why in Fig. 2(c) the approach of  $v_q$  towards the hydrodynamic value  $v_0$  could not be resolved, but only the approach towards  $v_\infty$  can be observed. Thus, the sound-velocity variation shown in Fig. 2(c) mostly reflects the microscopic contribution  $\Delta v_\mu$ .

In glass states, the  $\alpha$  process is arrested, and the hydrodynamic sound velocity is altered to  $\hat{v}_0 = v_0\sqrt{1+C}$ . There are at most  $\beta$  and  $\mu$  contributions to the sound-velocity increase from this hydrodynamic value. At and near  $T_c$ , the  $\beta$  contribution,  $\Delta v_\beta = v_\beta^+ - \hat{v}_0$ , cannot be neglected, where  $v_\beta^+ = v_0\sqrt{\Delta(\omega_\beta^+)}$  with  $\omega_\beta^+$  for glasses defined at the end of Sec. III B. This feature can be understood from Fig. 11(b), a redrawing of the inset of Fig. 3(a) with the logarithmic  $q$  axis, where the  $\beta$  contribution  $\Delta v_\beta$  and the microscopic contribution  $\Delta v_\mu$  (defined as the rest of the sound-velocity increase towards  $v_\infty$ ) are marked by vertical arrows. The  $\beta$ -relaxation contribution  $\Delta v_\beta$  cannot be resolved with the linear- $q$  axis, and this explains why in Fig. 3(a) the approach of  $v_q$  towards  $\hat{v}_0$  with decreasing  $q$  is retarded.

For temperatures further away from  $T_c$ , the  $\beta$ -relaxation contribution becomes smaller, and the sound-velocity increase from  $\hat{v}_0$  is entirely due to the microscopic process. This explains why in Fig. 3(b) the approach of  $v_q$  towards  $\hat{v}_0$  can be observed for  $T = 1.47$  even with the linear- $q$  axis. By further decreasing the temperature to  $T = 0.5$ , a new feature shows up reflecting the dominant harmonic nature in the stiff-glass-state dynamics. As discussed in connection with Fig. 10, there

appears a frequency interval where  $\Delta(\omega)$  becomes smaller than  $\Delta(\omega = 0)$ . According to Eq. (24b), this gives rise to a “negative” dispersion, and explains the result for  $T = 0.5$  shown in Fig. 3(c).

#### IV. LOW-FREQUENCY EXCITATIONS IN LONGITUDINAL AND TRANSVERSAL CURRENT SPECTRA

The evolution of the AOP is related to the arrest of density fluctuations caused by the cage effect, and the AOP is the result of a mapping of the cage distribution on the frequency axis (*cf.* Sec. III C). Since the arrest of density fluctuations is driven by the ones with a wave number  $q$  near the structure-factor-peak position [28], this interpretation of the AOP suggests that it appears in spectra of all probing variables that couple to density fluctuations of short wavelengths. But different probing variables will weight the oscillating complexes differently, and therefore the shape and the peak position of the AOP will depend somewhat on the probe. Two such examples have been analyzed in Ref. [24]: the tagged-particle density correlators and the velocity correlator  $\Psi(t)$ . In particular, it has been shown there how the AOP in the memory-kernel spectrum  $\hat{m}_s''(\omega)$  for  $\Psi(t)$  (*cf.* Fig. 7(c)) accounts for the excess intensity in the density of states  $2\Psi''(\omega)/\pi$  with respect to the Debye model.

In this section, we investigate how the AOP manifests itself in spectral features of the longitudinal and transversal current spectra. This issue is relevant since in recent computational studies [8, 10] two excitations have been observed in the longitudinal current spectra, but the low-frequency boson-peak-like excitations have been assigned to the transversal mode. Since there is no direct cross correlation between the longitudinal and transversal current dynamics, the appearance of the transversal mode in the longitudinal spectra is interpreted as being due to “mixing” phenomena [18]. This is in contrast to the above interpretation of the AOP, according to which possible low-frequency excitations in both of the longitudinal and transversal current spectra should be the manifestation of the AOP. Indeed, the AOP is present also in the memory kernel for the transversal current correlators, and its spectral features are quite similar to the one for the longitudinal current correlators as can be inferred from Fig. 7(c). To corroborate our statement, we will also study the density dependence of spectral features, because such study was claimed to support the interpretation in terms of the mixing of the longitudinal and transversal modes (*cf.* Sec. I).

##### A. Manifestation of AOP in spectral features

We present with solid lines in Fig. 12 typical density fluctuation spectrum  $\hat{\phi}_q''(\omega)$ , longitudinal current spectrum  $\phi_q^{L''}(\omega)$ , and transversal current spectrum  $\phi_q^{T''}(\omega)$

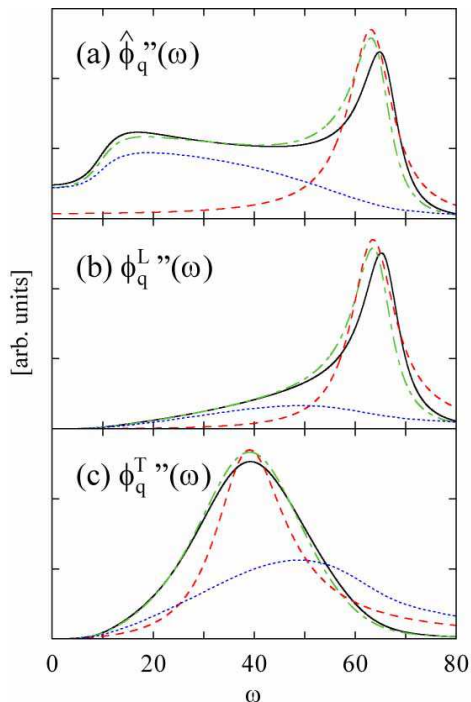


FIG. 12: (a) Density fluctuation spectrum  $\hat{\phi}_q''(\omega)$ , (b) longitudinal current spectrum  $\phi_q^{L''}(\omega)$ , and (c) transversal current spectrum  $\phi_q^{T''}(\omega)$  at wave number  $q = 3.7$  for  $\rho = 1.093$  and  $T = 0.5$ . Solid lines are based on the full MCT equations of motion described in Sec. II. Dash-dotted lines show curves within the generalized hydrodynamic description, Eqs. (34). Dashed lines denote the HFS part based on Eqs. (35), whereas dotted lines refer to the AOP portion from Eqs. (36). Curves for  $\hat{\phi}_q''(\omega)$  are obtained from those for  $\phi_q^{L''}(\omega)$  via Eq. (13).

at deep in the glass state,  $T = 0.5 \ll T_c$ . These results are based on the full MCT equations of motion described in Sec. II. The wave number  $q = 3.7$  chosen for the demonstration is about half of the structure-factor-peak position (*cf.* Fig. 1). The fluctuation spectrum  $\hat{\phi}_q''(\omega)$  shown in Fig. 12(a) exhibits two peaks for  $\omega \gtrsim 10$ , and illustrates a hybridization of the high-frequency sound with the modes building the AOP [24]: the narrow peak located at higher frequency is due to the high-frequency sound propagation, and a broad lower-frequency excitation reflects the AOP studied in Sec. III C. On the other hand, there is apparently only one peak in the longitudinal current spectrum  $\phi_q^{L''}(\omega)$  shown in Fig. 12(b). It is due to the high-frequency sound, and the peak position  $\omega_q^{L \max}$  is nearly the same as the one for the fluctuation spectrum. It is not clear how the AOP manifests itself in the spectral shape of  $\phi_q^{L''}(\omega)$  since, compared to  $\hat{\phi}_q''(\omega)$ , the low frequency part is suppressed due to the presence of the factor  $\omega^2$  (*cf.* Eq. (13)). The transversal current spectrum  $\phi_q^{T''}(\omega)$  shown in Fig. 12(c) also exhibits only one peak. Its peak frequency  $\omega_q^{T \max}$  is located at a lower frequency than  $\omega_q^{L \max}$  reflecting a smaller transversal sound velocity  $\omega_q^{T \max}/q$  compared to the longitudinal

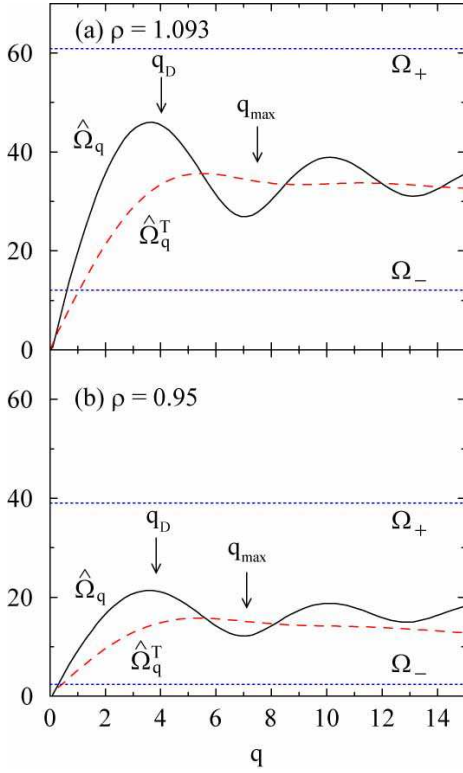


FIG. 13: Bare dispersion relation  $\hat{\Omega}_q$  for the longitudinal sound (solid line) and  $\hat{\Omega}_q^T$  for the transversal sound (dashed line) at  $T = 0.5$  for  $\rho = 1.093$  (a) and  $\rho = 0.95$  (b). Horizontal dotted lines denote the threshold frequencies  $\Omega_{\pm}$  (*cf.* Fig. 14), and arrows mark the Debye wave number  $q_D$  and the structure-factor-peak position  $q_{\max}$ .

one. Again, it is not clear whether there is a contribution to the spectral shape of  $\phi_q^{T''}(\omega)$  from the AOP. It is the purpose of this subsection to clarify this point.

To this end, we will derive approximate formulas specialized to describe each of the high-frequency-sound (HFS) and low-frequency-AOP portions of the spectra. The starting point is the following expression under the generalized hydrodynamic description (*cf.* Eq. (22) and citation [34]), obtained from Eq. (14) with the hatted memory kernel  $\hat{m}_q(\omega)$  approximated by its  $q \rightarrow 0$  limit,  $\hat{m}(\omega) = \hat{m}_{q=0}(\omega)$ :

$$\phi_q^{L''}(\omega) = \frac{\omega^2 \hat{\Omega}_q^2 \hat{m}''(\omega)}{[\omega^2 - \hat{\Omega}_q^2 \hat{\Delta}(\omega)]^2 + [\omega \hat{\Omega}_q^2 \hat{m}''(\omega)]^2}. \quad (34a)$$

Here  $\hat{\Delta}(\omega) = 1 - \omega \hat{m}'(\omega)$ . Corresponding description for the fluctuation spectrum  $\hat{\phi}_q''(\omega)$  is derived via Eq. (13). The formula (34a) describes hybridization of two oscillations: one is a bare sound with dispersion  $\hat{\Omega}_q$ , whose wave-number dependence is shown in Fig. 13(a), and the other is represented by the AOP spectrum in  $\hat{m}''(\omega)$ . The AOP region in the spectrum  $\hat{m}''(\omega)$  shall be defined as  $\Omega_- < \omega < \Omega_+$  in terms of the threshold frequencies  $\Omega_{\pm}$  introduced via the SGA spectrum in Sec. III C. These

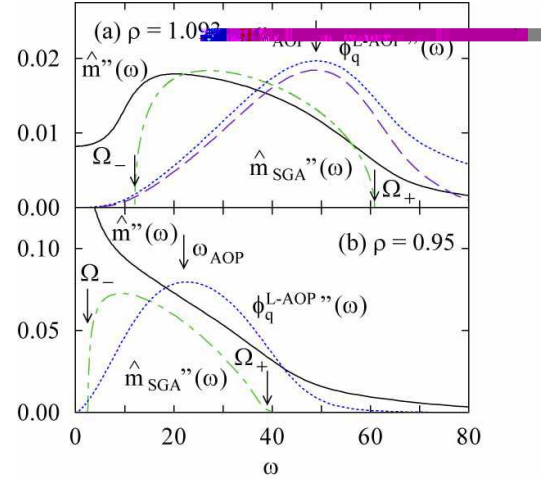


FIG. 14: (a) Solid line denotes the memory-kernel spectrum  $\hat{m}(\omega)$  for  $\rho = 1.093$  and  $T = 0.5$ , while dash-dotted line refers to the SGA spectrum based on Eqs. (31). Arrows mark the threshold frequencies  $\Omega_{\pm}$  defined below Eqs. (31). Dotted line denotes the frequency dependence of the function  $\phi_q^{L-AOP''}(\omega)$  given in Eq. (36a) in arbitrary units, and its peak frequency  $\omega_{AOP}$  is marked by an arrow. Long dashed line denotes the corresponding result based on Eq. (37a). (b) The same as in (a), but for  $\rho = 0.95$  [37].

frequencies are marked in Fig. 14(a). The hybridization occurs in the range  $\Omega_- < \hat{\Omega}_q < \Omega_+$  indicated in Fig. 13(a) where the two oscillations overlap. The generalized hydrodynamic description for the transversal current can be introduced similarly on the basis of Eq. (18):

$$\phi_q^{T''}(\omega) = \frac{\omega^2 (\hat{\Omega}_q^T)^2 \hat{m}_T''(\omega)}{[\omega^2 - (\hat{\Omega}_q^T)^2 \hat{\Delta}_T(\omega)]^2 + [\omega (\hat{\Omega}_q^T)^2 \hat{m}_T''(\omega)]^2}. \quad (34b)$$

Here  $\hat{m}_T(\omega) = \hat{m}_{q=0}^T(\omega)$  and  $\hat{\Delta}_T(\omega) = 1 - \omega \hat{m}_T'(\omega)$ . Since  $\hat{m}''(\omega) \approx \hat{m}_{q=0}''(\omega)$  as shown in Fig. 7(c), one understands that the hybridization of the bare transversal sound of dispersion  $\hat{\Omega}_q^T$  with the AOP occurs also in the range  $\Omega_- < \hat{\Omega}_q^T < \Omega_+$  indicated in Fig. 13(a). Figure 12 demonstrates that the generalized hydrodynamic description (dash-dotted lines) reproduce main features of all spectra fairly well. In particular, the subtle hybridization of the high-frequency sound and the AOP for  $\hat{\phi}_q''(\omega)$  is treated semiquantitatively correctly, justifying the use of Eqs. (34) as starting equations.

The HFS portion of  $\phi_q^{L''}(\omega)$  shall be approximated by a Lorentzian (multiplied by  $\omega^2$ ) with the width determined at the peak frequency  $\omega_q^{L \max}$ :

$$\phi_q^{L-HFS''}(\omega) = \frac{\omega^2 \hat{\Omega}_q^2 \hat{m}''(\omega_q^{L \max})}{[\omega^2 - (\omega_q^{L \max})^2]^2 + [\omega \hat{\Omega}_q^2 \hat{m}''(\omega_q^{L \max})]^2}. \quad (35a)$$

The dashed curve in Fig. 12(b) shows the result based on this formula, and the corresponding HFS curve for the fluctuation spectrum  $\propto \phi_q^{L-HFS''}(\omega)/\omega^2$  is included in

Fig. 12(a). One understands that the formula (35a) well describes the HFS portion of these spectra. Thus, the rest of the spectral intensity in the low-frequency regime should be due to the AOP.

Corresponding expression for the HFS part of the transversal current spectrum reads

$$\phi_q^{\text{T-HFS}''}(\omega) = \frac{\omega^2 (\hat{\Omega}_q^{\text{T}})^2 \hat{m}_T''(\omega_q^{\text{Tmax}})}{[\omega^2 - (\omega_q^{\text{Tmax}})^2]^2 + [\omega (\hat{\Omega}_q^{\text{T}})^2 \hat{m}_T''(\omega_q^{\text{Tmax}})]^2}. \quad (35b)$$

Figure 12(c) shows that this formula (dashed line) fairly catches the main peak of the spectrum, but the predicted width is considerably narrower than the one of the full MCT solution (solid line). This feature can be understood in terms of the AOP contribution as follows. We first notice that  $\omega_q^{\text{Tmax}} \approx 39$  for  $q = 3.7$  is located in the central region of the AOP (*cf.* Fig. 14(a)). Let us introduce frequencies  $\tilde{\omega}_{\pm}$  in this central regime so that  $\tilde{\omega}_- < \omega_q^{\text{Tmax}} < \tilde{\omega}_+$ . Since there holds  $\hat{m}_T''(\omega) \approx \hat{m}''(\omega)$  as shown in Fig. 7(c), the Kramers-Kronig relation implies  $\hat{\Delta}_T(\omega) \approx \hat{\Delta}(\omega)$ . One therefore understands from Fig. 10 that  $\hat{\Delta}_T(\omega)$  in the central regime of the AOP increases with  $\omega$ , i.e.,  $\hat{\Delta}_T(\tilde{\omega}_-) < \hat{\Delta}_T(\omega_q^{\text{Tmax}}) < \hat{\Delta}_T(\tilde{\omega}_+)$ . Since in lowest order  $\omega_q^{\text{Tmax}}$  is the solution to the equation  $(\omega_q^{\text{Tmax}})^2 = (\hat{\Omega}_q^{\text{T}})^2 \Delta_T(\omega_q^{\text{Tmax}})$  (*cf.* Eq. (23)), one has  $(\hat{\Omega}_q^{\text{T}})^2 \Delta_T(\tilde{\omega}_-) < (\omega_q^{\text{Tmax}})^2 < (\hat{\Omega}_q^{\text{T}})^2 \Delta_T(\tilde{\omega}_+)$ . Combined with  $\tilde{\omega}_-^2 < (\omega_q^{\text{Tmax}})^2 < \tilde{\omega}_+^2$ , this leads to an inequality  $[\tilde{\omega}_{\pm}^2 - (\omega_q^{\text{Tmax}})^2]^2 > [\tilde{\omega}_{\pm}^2 - (\hat{\Omega}_q^{\text{T}})^2 \Delta_T(\tilde{\omega}_{\pm})]^2$ . We also notice from Fig. 7(c) that there is only a weak  $\omega$  dependence in  $\hat{m}_T''(\omega)$  in the central regime of the AOP. All this together, one finds on the basis of Eqs. (34b) and (35b):  $\phi_q^{\text{T}''}(\tilde{\omega}_{\pm}) > \phi_q^{\text{T-HFS}''}(\tilde{\omega}_{\pm})$ . This way, one understands that the residual intensity in Fig. 12(c) which cannot be described as the HFS portion (dashed line) is caused by the frequency dependence of  $\hat{\Delta}_T(\omega)$  near  $\omega_q^{\text{Tmax}}$ , which in turn is due to the AOP. From the mentioned reasoning, it is clear that such deviation from the Lorentzian shape of the spectrum occurs whenever the sound resonance frequency is located in the central regime of the AOP. This explains why such deviation is small for the longitudinal current spectrum shown in Fig. 12(b), whose resonance frequency  $\omega_q^{\text{Lmax}} \approx 65$  exceeds  $\Omega_+$  and is not located in the central regime of the AOP. Such larger resonance frequency  $\omega_q^{\text{Lmax}}$  than expected from the bare dispersion  $\hat{\Omega}_q$  for  $q = 3.7$  shown in Fig. 13(a) is due to the positive dispersion discussed in Sec. III.

In view of the results presented so far, one understands that there are residual spectral intensities due to the AOP in the frequency regime  $\omega < \omega_q^{\text{L(T)max}}$ . In the following, we will derive approximate formulas extracting such AOP portion based on Eqs. (34). For this purpose, let us consider the denominator on the right-hand side of Eq. (34a),  $[\omega^2 - \hat{\Omega}_q^2 \hat{\Delta}(\omega)]^2 + [\omega \hat{\Omega}_q^2 \hat{m}''(\omega)]^2$ . The appearance of the HFS peak is mainly due to the decrease of the first term towards zero approaching the resonance position  $\omega_q^{\text{Lmax}}$ . Since we are interested in the off-resonant

regime  $\omega < \omega_q^{\text{Lmax}}$ , this term will be approximated by its the small- $\omega$  limit,  $[\omega^2 - \hat{\Omega}_q^2 \hat{\Delta}(\omega)]^2 \approx \hat{\Omega}_q^4$ . Correspondingly, only the leading-order contribution for small  $\omega$  shall be retained in the second term,  $[\omega \hat{\Omega}_q^2 \hat{m}''(\omega)]^2 \approx [\omega \hat{\Omega}_q^2 \hat{m}''(\omega = 0)]^2$ . This results in the following expression for possible AOP portion in  $\phi_q^{\text{L}''}(\omega)$ :

$$\phi_q^{\text{L-AOP}''}(\omega) = \frac{1}{\hat{\Omega}_q^2} \frac{\omega^2 \hat{m}''(\omega)}{1 + [\omega \hat{m}''(\omega = 0)]^2}. \quad (36a)$$

According to the derived formula, the  $q$  and  $\omega$  dependences are factorized. This implies that the peak position of the AOP portion – when it is visible – is  $q$  independent. The frequency dependence of the formula (36a) is shown as dotted line in Fig. 14(a), and its peak frequency, to be denoted as  $\omega_{\text{AOP}}$ , is marked by an arrow. Furthermore, one infers from the  $q$  dependence of  $\hat{\Omega}_q$  shown in Fig. 13 that the intensity of the AOP portion is predicted to increase upon increase of the wave number for  $q \lesssim q_D$ , whereas this trend becomes reversed for  $q \gtrsim q_D$ . Corresponding formula for the transversal current spectrum can be derived starting from Eq. (34b):

$$\phi_q^{\text{T-AOP}''}(\omega) = \frac{1}{(\hat{\Omega}_q^{\text{T}})^2} \frac{\omega^2 \hat{m}_T''(\omega)}{1 + [\omega \hat{m}_T''(\omega = 0)]^2}. \quad (36b)$$

Since  $\hat{m}_T''(\omega) \approx \hat{m}''(\omega)$  (*cf.* Fig. 7(c)), Eqs. (36) imply that the peak positions of the AOP portions of both longitudinal and transversal current spectra – when they are visible – are located at the same frequency  $\omega_{\text{AOP}}$ . Furthermore, a stronger intensity of the AOP portion is predicted for the transversal current spectra in the pseudo first Brillouin zone since there holds  $\hat{\Omega}_q > \hat{\Omega}_q^{\text{T}}$  as can be seen from Fig. 13(a). Finally, we notice that it is reasonable to further approximate the above formulas as

$$\phi_q^{\text{L-AOP}''}(\omega) = \frac{1}{\hat{\Omega}_q^2} \frac{\omega^2 \hat{m}^{(1)''}(\omega)}{1 + [\omega \hat{m}^{(2)''}(\omega = 0)]^2}, \quad (37a)$$

$$\phi_q^{\text{T-AOP}''}(\omega) = \frac{1}{(\hat{\Omega}_q^{\text{T}})^2} \frac{\omega^2 \hat{m}_T^{(1)''}(\omega)}{1 + [\omega \hat{m}_T^{(2)''}(\omega = 0)]^2}, \quad (37b)$$

since it is the one-mode contribution which provides the dominant contribution to the memory kernel and which describes the AOP, whereas the two-mode contribution provides a background spectrum as discussed in Sec. III C. Figure 14(a) demonstrates that indeed the difference between the curves based on Eqs. (36) and (37) is small. Our motivation for introducing Eqs. (37) will become clear in the next subsection.

The dotted lines in Fig. 12 are based on Eqs. (36). For the density fluctuation spectrum (Fig. 12(a)), it is seen that the dotted line, obtained from Eq. (36a) via the relation (13), extracts the AOP portion quite reasonably. It is also seen from Fig. 12(b) that Eq. (36a) provides a reasonable account of the residual low-frequency intensity in the longitudinal current spectrum located at  $\omega \approx \omega_{\text{AOP}}$ . Notice that the AOP appears differently in  $\hat{\phi}_q''(\omega)$  and

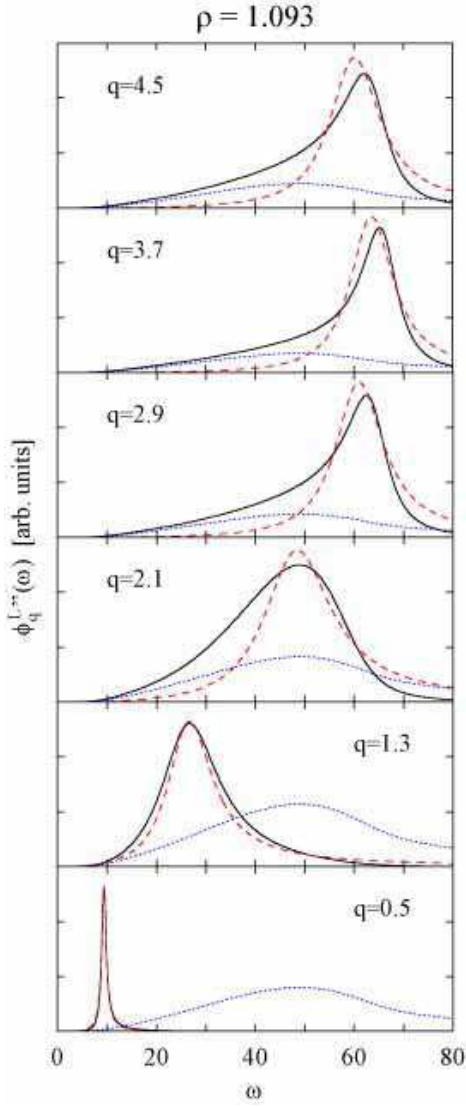


FIG. 15: Longitudinal current spectra  $\phi_q^{L''}(\omega)$  (solid lines) at  $\rho = 1.093$  and  $T = 0.5$  for indicated wave numbers. Dashed lines denote the HFS part based on Eq. (35a), whereas dotted lines refer to the AOP portion obtained from Eq. (36a).

$\phi_q^{L''}(\omega)$  reflecting the difference of the factor  $\omega^2$ . To understand the result shown in Fig. 12(c) for the transversal current spectrum, we notice that, by construction, the applicability of the formula (36b) is limited to the small- $\omega$  regime considerably lower than the sound resonance position  $\omega_q^{T\max}$ . Therefore, the dotted line in Fig. 12(c) in the region  $\omega \gtrsim \omega_q^{T\max}$  has no physical meaning. Nevertheless, it is seen that the dotted line accounts for the residual intensity in the low-frequency regime which cannot be described as the HFS portion (dashed line). Thus, Eq. (36b) describes the low-frequency part of the deviation from the Lorentzian shape explained above.

The variation of the longitudinal and transversal current spectra (solid lines) with changes of wave number  $q$  is presented in Figs. 15 and 16, along with their decom-

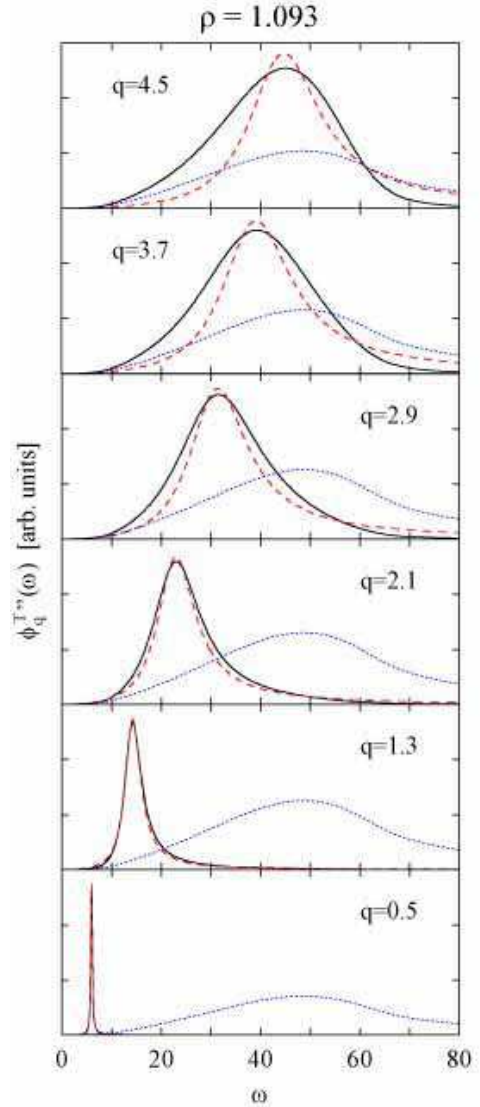


FIG. 16: Transversal current spectra  $\phi_q^{T''}(\omega)$  (solid lines) at  $\rho = 1.093$  and  $T = 0.5$  for indicated wave numbers. Dashed lines denote the HFS part based on Eq. (35b), whereas dotted lines refer to the AOP portion obtained from Eq. (36b).

position into the HFS part (dashed lines) and possible AOP portion (dotted lines). The dispersion relation and the full width at half maximum (FWHM) as a function of  $q$  are summarized in Fig. 17. We start from the discussion on the longitudinal current spectra. When  $q$  is small so that  $\omega_q^{L\max} < \Omega_-$ , there is practically no effect from the AOP on the spectral shape. (However, the AOP affects the resonance frequency  $\omega_q^{L\max}$  near  $\Omega_-$  as discussed in Sec. III D.) Therefore, the spectrum for  $q = 0.5$  shown in Fig. 15 is dominated by the HFS portion (dashed line), and there is no physical meaning in the dotted line for this  $q$  value. Thus, the spectrum for  $q = 0.5$  is very close to Lorentzian (multiplied by  $\omega^2$ ), and its width agrees with the one from the hydrodynamic prediction  $q^2 \hat{v}_0^2 \hat{n}''(\omega = 0)$  as demonstrated in Fig. 17(b). As

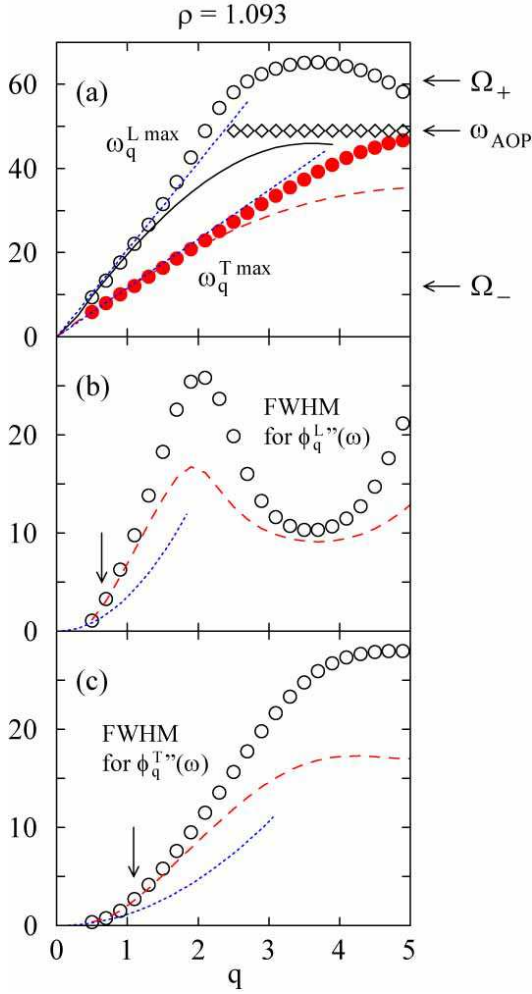


FIG. 17: (a) Peak positions  $\omega_q^{L \max}$  of  $\phi_q^{L''}(\omega)$  (open circles) and  $\omega_q^{T \max}$  of  $\phi_q^{T''}(\omega)$  (filled circles) as a function of  $q$  for  $\rho = 1.093$  and  $T = 0.5$ . Solid and dashed lines denote the bare dispersions  $\hat{\Omega}_q$  and  $\hat{\Omega}_q^T$ , respectively. Dotted lines exhibit the hydrodynamic dispersion laws  $q\hat{v}_0$  and  $q\hat{v}_0^T$ . Peak positions of the AOP portion in  $\phi_q^{L''}(\omega)$  are denoted by open diamonds. Horizontal arrows mark  $\Omega_{\pm}$  and  $\omega_{\text{AOP}}$  taken from Fig. 14(a). (b) Full width at half maximum (FWHM) for  $\phi_q^{L''}(\omega)$  (circles) as a function of  $q$ . Dashed line denotes the Lorentzian width  $\hat{\Omega}_q^2 \hat{m}''(\omega_q^{L \max})$  predicted by Eq. (35a). Dotted line refers to the hydrodynamic width,  $q^2 \hat{v}_0^2 \hat{m}''(\omega = 0)$ . Vertical arrow marks the wave number where  $\omega_q^{L \max} = \Omega_-$  holds. (c) The same as in (b), but for  $\phi_q^{T''}(\omega)$  for which the Lorentzian width (dashed line) is given by  $(\hat{\Omega}_q^T)^2 \hat{m}''(\omega_q^{T \max})$  and the hydrodynamic width (dotted line) by  $q^2 (\hat{v}_0^T)^2 \hat{m}''(\omega = 0)$ . Vertical arrow marks the wave number where  $\omega_q^{T \max} = \Omega_-$  holds.

$q$  increases so that  $\omega_q^{L \max}$  becomes larger than  $\Omega_-$ , effects from the AOP set in. These effects increase the spectral width, as exemplified for  $q = 1.3$  and  $2.1$  in Fig. 15, in two ways. First, the width becomes larger compared to the hydrodynamic width because  $\hat{m}''(\omega_q^{L \max}) > \hat{m}''(\omega = 0)$  when the resonance frequency  $\omega_q^{L \max}$  is located in the AOP regime,  $\Omega_- < \omega_q^{L \max} < \Omega_+$  (cf. Fig. 14(a)). This

shows up as the deviation of the dashed line from the dotted line in Fig. 17(b). In addition, the frequency dependence of  $\hat{\Delta}(\omega)$ , which again is caused by the AOP, also enlarges the width as explained above in connection with Fig. 12(c). This latter effect leads to the non-Lorentzian shape of the spectrum, i.e., the deviation of the solid line from the dashed line for  $q = 1.3$  and  $2.1$  shown in Fig. 15, and also explains the difference between corresponding circles and dashed line in Fig. 17(b). The dotted lines in Fig. 15 account for the low-frequency part of the non-Lorentzian spectra as discussed above. As  $q$  is increased further, the positive dispersion effect becomes important, and it pushes  $\omega_q^{L \max}$  considerably above frequencies expected from the bare dispersion  $\hat{\Omega}_q$  as shown in Fig. 17(a). Thereby, there opens a frequency window, where  $\omega_{\text{AOP}} < \omega_q^{L \max}$  holds and the appearance of the AOP itself can be observed in the spectra. This feature holds  $q \gtrsim 2.9$  as shown in Fig. 15. As mentioned above, there is no  $q$  dependence in  $\omega_{\text{AOP}}$ , which results in flat dispersion curve for the low-frequency excitations as demonstrated with open diamonds in Fig. 17(a).

Corresponding results for the transversal current spectra shown in Figs. 16 and 17 can be explained similarly. But here, the positive dispersion of  $\omega_q^{T \max}$  from the hydrodynamic law  $q\hat{v}_0^T$  with  $\hat{v}_0^T = v_0 \sqrt{C_{q=0}^T}$ , obtained from the leading-order expansion of  $\hat{\Omega}_q^T$ , is not so strong as in the longitudinal case. This is because the bare transversal sound dispersion  $\hat{\Omega}_q^T$  for  $q \lesssim q_D$  is located below the maximum frequency  $\omega \approx 40$  of the the susceptibility spectrum  $\omega \hat{m}''(\omega)$  (cf. the bottom panel for  $T = 0.5$  in Fig. 8), where the positive dispersion effect is most significant as explained in Sec. III. Thus, there is no frequency regime where  $\omega_{\text{AOP}} < \omega_q^{T \max}$  holds for the transversal current spectra, which can be inferred from Fig. 17(a). Therefore, only the width of  $\phi_q^{T''}(\omega)$  is affected by the AOP, which is summarized in Fig. 17(c). However, this feature is altered when the density is decreased, as we will see in the next subsection.

## B. Longitudinal and transversal current spectra at lower density

In this subsection, effects of varying density on spectral features of the longitudinal and transversal current spectra shall be investigated. Specifically, a density  $\rho = 0.95$  lower than  $1.093$  studied so far will be considered, but with temperature  $T = 0.5$  fixed.

Upon decrease of the density, the bare sound dispersions  $\hat{\Omega}_q$  and  $\hat{\Omega}_q^T$  and the memory-kernel spectrum  $\hat{m}''(\omega)$  are shifted to lower frequencies as demonstrated in Figs. 13(b) and 14(b), respectively. Notice the striking similarity between the change in  $\hat{m}''(\omega)$  upon decrease of the density at fixed  $T$  and the change upon increase of the temperature at fixed  $\rho$  found in Fig. 7(b). Indeed, the critical temperature is decreased to  $T_c \approx 0.644$  for  $\rho = 0.95$ , and lowering the density at fixed  $T = 0.5$  drives

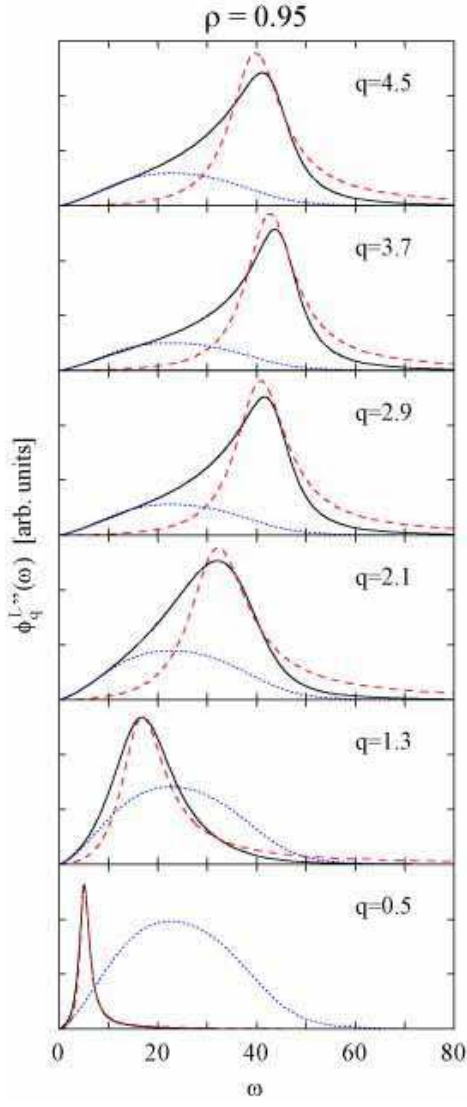


FIG. 18: The same as in Fig. 15, but for a lower density  $\rho = 0.95$ , and dotted lines referring to the AOP portion are based on Eq. (37a) as discussed in text.

the system closer to the critical point. As discussed with Fig. 7(b), a strong central peak is formed when the system approaches the critical point, and the modes building the AOP get buried under its tail. But again, Fig. 14(b) demonstrates that the SGA kernel  $\hat{m}_{\text{SGA}}''(\omega)$  extracts the buried AOP portion quite reasonably [37]. Thus, in analogy to what is found in Fig. 7(b), the AOP shifts towards lower frequencies upon decrease of the density, accompanied by an increase of its spectral intensity.

As a related problem, we found that the use of Eqs. (36) to extract the AOP portion from current spectra leads to unplausible results. This is because of the mentioned development of the central peak, leading to quite large value of  $\hat{m}''(\omega = 0)$ . As will be demonstrated in the following (*cf.* Figs. 20(b) and 20(c)), such large value of  $\hat{m}''(\omega = 0)$  caused by the critical decay near  $T_c$  is

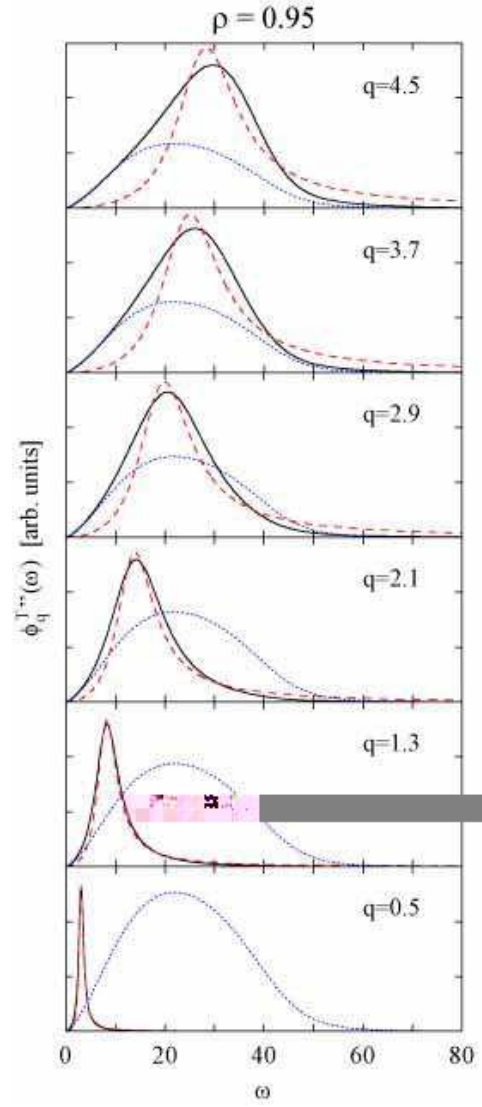


FIG. 19: The same as in Fig. 16, but for a lower density  $\rho = 0.95$ , and dotted lines referring to the AOP portion are based on Eq. (37b) as discussed in text.

not appropriate for handling the high-frequency dynamics. We will therefore use Eqs. (37) instead of Eqs. (36), which essentially amounts to replacing  $\hat{m}''(\omega = 0)$  with  $\hat{m}^{(2)''}(\omega = 0)$ . The curves based on Eqs. (37) are not much affected by the critical dynamics because (i) only corrections to the critical decay enter into  $\hat{m}^{(2)''}(\omega)$  as explained in connection with Fig. 7(b), and (ii) the critical-decay contribution in  $\hat{m}^{(1)''}(\omega)$  is suppressed in Eq. (37a) due to the presence of the factor  $\omega^2$  in its denominator. As demonstrated in Fig. 14(a), there is practically no difference between the use of Eqs. (36) and (37) for  $\rho = 1.093$ , and we expect that physics is not altered with the use of the latter for  $\rho = 0.95$ .

Longitudinal and transversal current spectra for  $\rho = 0.95$  (solid lines) with changes of wave number  $q$  are presented in Figs. 18 and 19, along with their decomposition

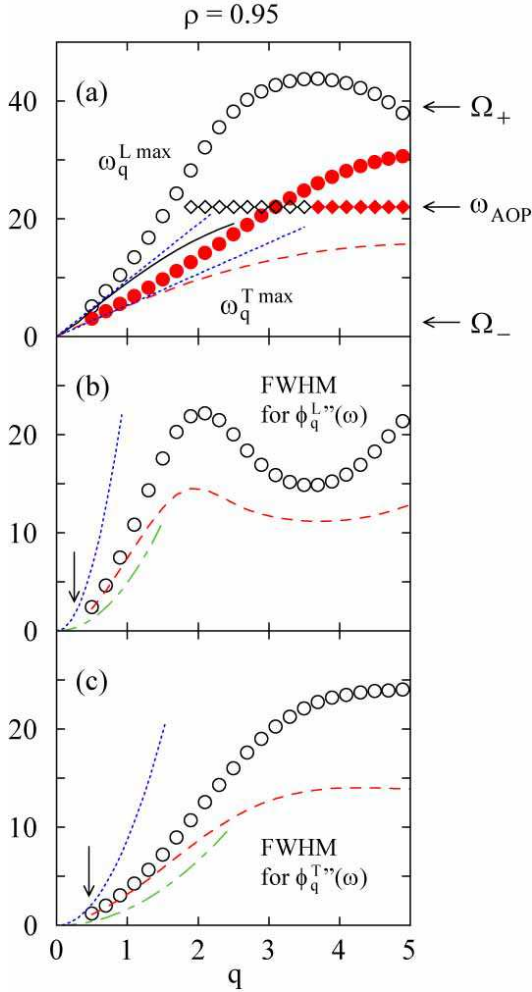


FIG. 20: The same as in Fig. 17, but for a lower density  $\rho = 0.95$ . In (a), filled diamonds are added denoting the peak positions of the AOP portion in  $\phi_q^{T''}(\omega)$ . Dash-dotted lines are added in (b) and (c) denoting  $q^2 \hat{v}_0^2 \hat{m}^{(2)''}(\omega = 0)$  and  $q^2 (\hat{v}_0^T)^2 \hat{m}_T^{(2)''}(\omega = 0)$ , respectively (see text for details).

into the HFS part (dashed lines) and possible AOP portion (dotted lines). As mentioned above, the dotted lines in these figures are based on Eqs. (37). The dispersion relation and the FWHM as a function of  $q$  are summarized in Fig. 20. It is seen from Figs. 20(b) and 20(c) that indeed the hydrodynamic prediction for the width with  $\hat{m}''(\omega = 0)$  does not work for  $\rho = 0.95$ ; instead, the corresponding prediction with  $\hat{m}^{(2)''}(\omega = 0)$  reasonably accounts for the width in the small- $q$  regime.

It is seen by comparing Figs. 15 and 18 that the AOP portion of the longitudinal current spectra for the smaller density  $\rho = 0.95$  is located at lower frequencies and its intensity is more enhanced. These differences simply reflect the shift of the AOP to lower frequencies accompanied by an increase of its spectral intensity for  $\rho = 0.95$ . In addition, the positive dispersion of the sound velocity and the deviation from the Lorentzian shape of the spectra start

at smaller  $q$  for  $\rho = 0.95$ , as can be inferred by comparing Figs. 17 and 20. These features are also due to the shift of the AOP to lower frequencies upon decrease of the density. Furthermore, there is no “negative” dispersion (*cf.* Sec. III D) for  $\rho = 0.95$  since the memory kernel for  $T = 0.5$  at this density is not dominated by the harmonic contributions (*cf.* Fig. 14(b)). Otherwise, the variation of the longitudinal current spectra with changes of  $q$  for  $\rho = 0.95$  is quite similar to the one found for  $\rho = 1.093$ , and the discussion shall not be repeated.

The variation of the transversal current spectra with changes of  $q$  for  $\rho = 0.95$  is also quite similar to the one found for  $\rho = 1.093$ , as can be understood by comparing Figs. 16 and 19. But here, the resonance frequency  $\omega_q^{T \max}$  of the transversal sound exhibits a strong positive dispersion as shown in Fig. 20(a). Again, this is caused by the shift of the AOP to lower frequencies. The positive dispersion of the transversal sound velocity due to the contribution from the AOP can be discussed quite similarly to what is presented in Sec. III for the longitudinal sound. Thereby, there opens a frequency window also for the transversal current spectra, where  $\omega_{\text{AOP}} < \omega_q^{T \max}$  holds and the appearance of the AOP itself can be observed in the spectra. Such AOP portion can be observed for  $q \gtrsim 3.7$  in Fig. 19, yielding a flat dispersion curve for the low-frequency excitations of the transversal current spectra as demonstrated with filled diamonds in Fig. 20(a). This is in contrast to the result found for  $\rho = 1.093$ , where  $\omega_{\text{AOP}} > \omega_q^{T \max}$  holds for the whole  $q$  range and the effects from the AOP showed up only in the width of the transversal current spectra.

## V. CONCLUDING REMARKS

In this paper, we presented a theoretical investigation on the high-frequency collective dynamics in liquids and glasses at microscopic length and time scales based on the MCT for ideal liquid-glass transition. We focused on recently investigated issues from IXS and computer-simulation studies for dynamic structure factors and longitudinal and transversal current spectra: the anomalous dispersion of the high-frequency sound velocity and the nature of the low-frequency excitation called the boson peak. The results of the theory are demonstrated for a model of the LJ system.

The MCT explains the evolution of the structural-relaxation processes as precursor of the glass transition at a critical temperature  $T_c$ , which is driven by the mutual blocking of a particle and its neighbors (cage effect) [23, 28]. On the other hand, the theory also predicts the development of the harmonic vibrational excitations in stiff-glass states  $T \ll T_c$ , called the AOP. The AOP is caused by the strong interaction between density fluctuations at microscopic length scales and the arrested glass structure, and exhibits the properties of the boson peak [24]. As demonstrated in Sec. III C, the AOP persists also near and above  $T_c$ , and considerable portion of

the microscopic process in systems ranging from high- $T$  liquids down to deep-in-glass states can be described as a superposition of harmonic vibrational dynamics. We investigated in Sec. III how the interference of the sound mode with these structural-relaxation processes and vibrational excitations shows up as anomalies in the sound-velocity dispersion.

In the vicinity of  $T_c$ , the structural-relaxation contributions to the sound-velocity dispersion show up at very small wave numbers, which can fully be appreciated only with the logarithmic  $q$  axis (*cf.* Fig. 11). Therefore, with the linear- $q$  axis adopted in conventional studies on the dispersion relation, the sound velocity  $v_q$  in the small- $q$  limit is located above the hydrodynamic value  $v_0$  (*cf.* Fig. 2(c)), and this even at  $T = 4.0$  (*cf.* Fig. 2(b)) which is more than twice of the critical temperature  $T_c$ . We notice that this temperature is also higher than the freezing temperature  $T_f \approx 3.3$  which is estimated based on the so-called Hansen-Verlet criterion [27]. Thus, except for very high temperature like  $T = 10$  (*cf.* Fig. 2(a)), the variation of the sound velocity  $v_q$  which is visible in the linear  $q$  axis basically reflects the contribution from the microscopic process. This theoretical result is in contrast to the traditional picture based on the viscoelastic model according to which the anomalous dispersion is fully ascribed to the structural relaxation, but is in agreement with finding from recent IXS studies on simple liquid metals near the melting temperature [12, 13, 14, 15, 16].

The description of the microscopic process in terms of the AOP – a superposition of harmonic oscillations of particles inside their cages – implies that the decay of the memory kernel at microscopic times  $\log_{10} t \lesssim -1$  (*cf.* Fig. 4) reflects the dephasing of different oscillatory components in the force fluctuations. This is in consistent with the implication from the computer-simulation study on harmonic glass [7]. Such microscopic process, despite arrested structural relaxations, accounts for the positive dispersion in glass states (*cf.* Fig. 3), whose presence has been reported from recent MD and IXS studies [6, 7, 8, 9, 10, 11]. That the microscopic process due to the AOP persists both in liquid and glass states with only weak temperature dependence of its characteristic time or frequency (*cf.* Fig. 8) is in accord with the computer-simulation result presented in Ref. [9].

To see further implications of the theory, we show in Fig. 21 the sound velocities  $v_q(T)$  as a function of  $T$  for fixed  $q = 10^{-2}$  (solid line) and  $q = 0.5$  (dash-dotted line). (The argument  $T$  shall be added here to emphasize the  $T$  dependence.) The density is fixed to  $\rho = 1.093$ , and  $v_q(T)$  are obtained from Eq. (24b) with  $\Delta(\omega)$  determined for each temperature (*cf.* Fig. 6). Assuming that LJ particles under study are of argon size ( $\approx 0.34$  nm), the wave number  $q = 0.5$  ( $1.5 \text{ nm}^{-1}$ ) is in the lowest momentum-transfer range in IXS measurements, and  $q = 10^{-2}$  ( $0.03 \text{ nm}^{-1}$ ) is a typical momentum transfer in Brillouin light scattering (BLS) experiments. As shown in Fig. 3(c) for a stiff-glass state  $T = 0.5$ , a negative dispersion is observable for  $q < 1$  where the sound velocity

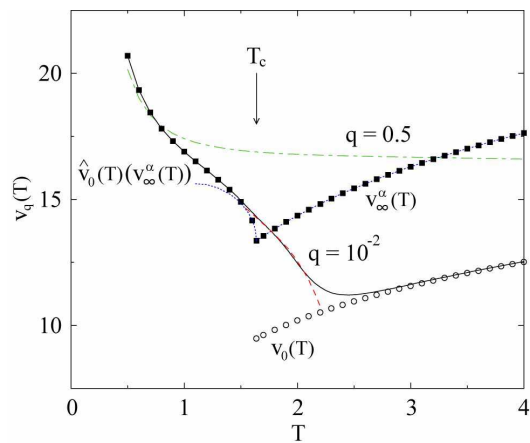


FIG. 21: Sound velocities  $v_q(T)$  as a function of  $T$  at  $\rho = 1.093$  for  $q = 10^{-2}$  (solid line) and  $q = 0.5$  (dash-dotted line), which are based on Eq. (24b) with  $\Delta(\omega)$  determined for each temperature (*cf.* Fig. 6). Hydrodynamic sound velocities  $v_0(T)$  for  $T > T_c$  and  $\hat{v}_0(T) = v_\infty^\alpha(T)$  (see text) for  $T \leq T_c$  are denoted as open circles and filled squares, respectively.  $v_\infty^\alpha(T)$  for  $T > T_c$ , given by  $v_\infty^\alpha(T) = v_0(T)/\sqrt{1-f_0^c}$ , are also denoted as filled squares. Dotted line shows the square-root singularity translated to  $v_\infty^\alpha(T)$ , i.e.,  $v_\infty^\alpha(T) = v_0(T)\sqrt{1-f_0(T)}$  with  $f_0(T) = f_0^c + h_0\sqrt{\sigma/(1-\lambda)}$  for  $T \leq T_c$  and  $f_0(T) = f_0^c$  for  $T > T_c$ . Dashed line exhibits the  $\beta$ -relaxation contribution to  $v_q(T)$  which is based on Eq. (24b) with  $\Delta(\omega)$  determined from the MCT asymptotic formula (30).

$v_q(T)$  is smaller than the hydrodynamic ( $q \rightarrow 0$ ) value. This is due to the dominant harmonic nature of the dynamics at  $T = 0.5$ , because of which there appears a frequency interval where  $\Delta(\omega)$  is smaller than its  $\omega \rightarrow 0$  limit (*cf.* Fig. 10). The presence of the negative dispersion is reflected in Fig. 21 as the emergence of the low- $T$  region where the IXS sound velocity ( $v_q(T)$  for  $q = 0.5$ ) is smaller than the BLS sound velocity ( $q = 10^{-2}$ ). Such  $T$  dependence of the IXS and BLS sound-velocity data in the low- $T$  region has been reported for glycerol [1, 38] (see Fig. 5(b) of Ref. [1]). Thus, there is an experimental result which is consistent with the presence of the negative dispersion predicted by the theory. That the difference between the IXS and BLS sound-velocity data in the low- $T$  region is smaller in Fig. 21 than the one found in Fig. 5(b) of Ref. [1] for glycerol and that such difference is not clearly observable in orthoterphenyl [39] might be rationalized by the stronger influence of vibrational modes (boson peaks) in the dynamics of network glass former glycerol than in fragile glass formers like the LJ system and orthoterphenyl [40]. According to this reasoning, the presence of the negative dispersion is also expected in strong glass formers like silica where the influence of vibrational dynamics is even stronger [40]. The sound velocity data for vitreous silica reported in Fig. 3 of Ref. [11] seems to indicate this possibility, but large error bars do not allow ones to draw a decisive conclusion. It would therefore be of value to re-analyze the data for silica with improved resolution.

Hydrodynamic sound velocities  $v_0(T)$  for  $T > T_c$  and  $\hat{v}_0(T) = v_0(T)/\sqrt{1-f_0(T)}$  for  $T \leq T_c$  are included in Fig. 21 as open circles and filled squares, respectively.  $v_0(T)$  increases with increasing  $T$  because in our study  $T$  is varied with density fixed, leading to increased pressures at elevated temperatures. On the other hand, the  $T$  dependence of  $\hat{v}_0(T)$  is dominated by that of  $f_0(T)$  (*cf.* Fig. 1), and this explains the increase of  $\hat{v}_0(T)$  with decreasing  $T$ . Here a side remark shall be added concerning the notion of the “hydrodynamic” sound velocity  $\hat{v}_0(T)$  for glass states referring to  $T \leq T_c$ . The MCT in its idealized form, adopted in the present study, predicts the structural arrest at the critical temperature  $T_c$  which is located above the calorimetric glass-transition temperature  $T_g$ . In reality there are slow dynamical processes – referred to as hopping processes – which restore ergodicity for  $T \leq T_c$ . These processes, which are studied within the extended version of the MCT [41], change the ideal elastic peaks  $\pi f_q(T)\delta(\omega)$  of density fluctuation spectra  $\phi_q''(\omega)$  into quasielastic  $\alpha$  peaks of nonzero width also for  $T \leq T_c$ .  $f_q(T)$  in real systems therefore has to be interpreted as an effective Debye-Waller factor [42], which can be measured as area under the quasielastic  $\alpha$  peak in  $\phi_q''(\omega)$  or by determining the plateau of the  $\phi_q(t)$ -versus- $\log t$  curve. Correspondingly,  $\hat{v}_0(T)$  should be interpreted as the extension of  $v_\infty^\alpha(T)$  – the sound velocity in the high-frequency limit of the  $\alpha$  regime – introduced in Sec. III D to  $T \leq T_c$ .  $v_\infty^\alpha(T)$  for  $T > T_c$  are given by  $v_\infty^\alpha(T) = v_0(T)/\sqrt{1-f_0^c}$  (*cf.* Sec. III D), and are also included with filled squares in Fig. 21:  $v_\infty^\alpha(T)$  defined below and above  $T_c$  merge at  $T_c$ .

The mentioned dependence of  $v_\infty^\alpha(T)$  on  $f_0(T)$  has been utilized to extract experimentally the zero wave-number limit of the Debye-Waller factor via the relation  $f_0(T) = 1 - [v_0(T)/v_\infty^\alpha(T)]^2$  [43, 44] and to test the square-root singularity as predicted by the MCT,  $f_0(T) = f_0^c + h_0\sqrt{\sigma/(1-\lambda)}$  for  $T \leq T_c$  and  $f_0(T) = f_0^c$  for  $T > T_c$  (*cf.* Eq. (4)). The dotted line in Fig. 21 shows the square-root singularity translated to  $v_\infty^\alpha(T)$ . In our system, there is no possibility to detect the singularity based on the IXS sound velocity ( $v_q(T)$  for  $q = 0.5$ ), which basically reflects the contribution from the microscopic process (*cf.* Fig. 11). On the other hand, the BLS sound velocity ( $q = 10^{-2}$ ) probes much lower momentum-transfer range, and is thus affected also by the structural-relaxation processes. In particular, the  $\beta$ -relaxation contribution to  $v_q(T)$  plays an important role in the vicinity of  $T_c$  (*cf.* Fig. 11), as can also be inferred by comparing the solid and dashed lines in Fig. 21, the latter being obtained based on Eq. (24b) with  $\Delta(\omega)$  determined from the MCT asymptotic formula (30) for the  $\beta$  relaxation. Thus, the  $\beta$  relaxation must be included for reliable determination of  $f_0(T)$  via the sound velocity data, which is in full agreement with the conclusion drawn in Ref. [44]. (*cf.* Fig. 13 of Ref. [44] where BLS data for  $\text{CaKNO}_3$  corresponding to solid line and filled squares in Fig. 21 are shown.)

We studied in Sec. IV how the AOP manifests itself

in the spectral shape of the glass-state longitudinal and transversal current spectra at low frequencies. For small wave numbers where the sound resonance frequencies are located below the low-frequency threshold of the AOP,  $\omega_q^{L(T)\max} < \Omega_-$ , there is practically no effect from the AOP, and the longitudinal and transversal current spectra are dominated by the sound excitations of the Lorentzian spectral shape. By increasing the wave numbers so that the sound resonance frequencies enter the AOP region,  $\Omega_- < \omega_q^{L(T)\max}$ , the hybridization of the sound mode with the AOP becomes important, and the shape of the current spectra deviates from Lorentzian. As the wave number is increased further, the interference of the sound mode with the AOP leads to the positive dispersion of the sound velocities, pushing  $\omega_q^{L(T)\max}$  considerably above frequencies expected from the bare dispersion. Thereby, there opens a frequency window, where the appearance of the AOP itself can be observed in the spectra at low frequencies. Furthermore, our approximate formulas (36) predict that (i) there is no  $q$  dependence in the peak frequency  $\omega_{\text{AOP}}$  of the AOP portions in the current spectra, (ii)  $\omega_{\text{AOP}}$  is nearly the same for both of the longitudinal and transversal current spectra since  $\hat{m}''(\omega) \approx \hat{m}_T''(\omega)$  as shown in Fig. 7(c), and (iii) the intensity of the AOP portion is stronger for the transversal current spectra than for the longitudinal ones in the pseudo first Brillouin zone. These theoretical predictions, demonstrated in Figs. 15 to 20 for the LJ system, are in agreement with previous findings from MD and IXS studies [8, 10, 11, 17]. Thus, the low-frequency excitations observable at the same resonance frequency  $\omega_{\text{AOP}}$  in both of the glass-state longitudinal and transversal current spectra are the manifestation of the AOP. Usually, the boson peaks are discussed below  $T_g$ . On the other hand, the glass state in the present paper refers to  $T \leq T_c$ . Since  $T_c$  is located above  $T_g$ , our theoretical results for glasses apply also for some ranges of the liquid state in the conventional terminology.

According to our theoretical results, it is essential to have the positive dispersion of the transversal sound velocity for the appearance of the low-frequency excitations in the transversal current spectra, whose presence has never been discussed so far. This comes out from our study on the density dependence of the dispersion relation, shown in Figs. 17(a) and 20(a) for the higher and the lower densities, respectively. Such density dependence of the dispersion relation is in accord with the one reported from the computer simulation for vitreous silica (*cf.* Fig. 4 of Ref. [10]). It would therefore be of value if simulation studies could test whether or not our theoretical prediction agrees with their data.

We notice that the intensity of the low-frequency excitations for the LJ system studied in this paper is weaker than the one, e.g., known from computer-simulation results on silica [8, 10]: the low-frequency excitations in the present study are shoulders rather than peaks. Again, this feature may be ascribed to the fact that the LJ system can be classified as a fragile glass former, in which

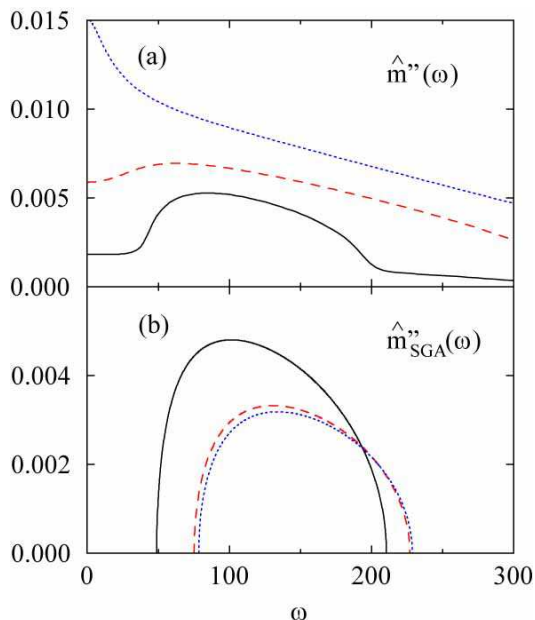


FIG. 22: (a) The memory-kernel spectrum  $\hat{m}''(\omega)$  and (b) the SGA spectrum  $\hat{m}_{SGA}''(\omega)$  obtained with the cutoff  $q^* = 40$  (solid lines), 80 (dashed lines), and 120 (dotted lines) for the hard-sphere system at packing fraction  $\varphi = 0.6$ . As in Ref. [24], the static structure factor  $S_q$  has been evaluated within the Percus-Yevick approximation, and the units of length and time have been chosen so that the hard-sphere diameter  $d = 1$  and the thermal velocity  $v = 2.5$ .

the boson peak is less pronounced than in strong glass formers like silica [40].

Finally, let us make a comment on the cutoff problem mentioned in Ref. [24]. As already noticed there, the MCT results for the hard-sphere system in stiff-glass states change if the cutoff  $q^*$  of the wave-number grids used in the calculations is varied. This is demonstrated in Fig. 22(a) showing the  $q^*$  dependence of the memory-kernel spectrum  $\hat{m}''(\omega)$  for the hard-sphere system at packing fraction  $\varphi = 0.6$  studied in Ref. [24]. It is seen that the intensity of  $\hat{m}''(\omega)$  increases with increasing  $q^*$ . Furthermore, the broad harmonic-oscillation “peak”

reflecting the AOP, observable in  $\hat{m}''(\omega)$  for the cutoff  $q^* = 40$  adopted in Ref. [24], disappears for  $q^* = 120$ ; it shows up only as a shoulder. Such  $q^*$  dependence reflects the slow decrease towards zero of the direct correlation function  $c_k$  of the hard-sphere system for  $k$  tending to infinity, because of which the relevant coupling coefficient  $V_k$  (cf. Eq. (2c)) does not approach zero even in the  $k \rightarrow \infty$  limit. However, this does not mean that there is no AOP in the hard-sphere system. As discussed in Sec. III C, the AOP portion of  $\hat{m}''(\omega)$ , even when it is buried under the tail of the quasielastic peak, is well extracted by the SGA spectrum  $\hat{m}_{SGA}''(\omega)$ . Figure 22(b) demonstrates that there is no  $q^*$  dependence in  $\hat{m}_{SGA}''(\omega)$  provided a sufficiently large  $q^*$  is chosen. In this sense, the AOP is well defined in the hard-sphere system. But, it does not show up as a peak in  $\hat{m}''(\omega)$  due to the two-mode contributions, which are neglected within the SGA. Thus, the increase of the intensity of  $\hat{m}''(\omega)$ , in particular, the smearing out of the “gap” for  $0 < \omega < \Omega_-$ , with increasing  $q^*$  is due to the development of the two-mode contributions. Because of the strong anharmonic effects, no harmonic-oscillation peak in the spectrum  $\hat{m}''(\omega)$  is expected for the hard-sphere system.

On the other hand, introducing the cutoff is equivalent to softening the hard-sphere potential. Indeed, we have confirmed that there is no cutoff problem in the LJ system considered in this paper, and that all the essential results presented in Ref. [24] can be reproduced for this system. In particular, one observes harmonic-oscillation peak for the LJ system in stiff-glass states as shown in Fig. 7(a), which is free from the mentioned cutoff problem. Thus, the whole physics discussed in Ref. [24] for stiff-glass states remain valid for systems where particles interact with regular interaction potentials.

### Acknowledgments

The author thanks W. Götze for valuable comments. This work was supported by Grant-in-Aids for scientific research from the Ministry of Education, Culture, Sports, Science and Technology of Japan (No. 17740282).

- 
- [1] F. Sette, M. Krisch, C. Masciovecchio, G. Ruocco, and G. Monaco, *Science* **280**, 1550 (1998).
  - [2] G. Ruocco and F. Sette, *J. Phys.: Condens. Matter* **13**, 9141 (2001).
  - [3] T. Scopigno and G. Ruocco, *Rev. Mod. Phys.* **77**, 881 (2005).
  - [4] J.-P. Hansen and I. R. McDonald, *Theory of Simple Liquids* (Academic Press, London, 1986), 2nd ed.
  - [5] U. Balucani and M. Zoppi, *Dynamics of the Liquid State* (Clarendon Press, Oxford, 1994).
  - [6] S. N. Taraskin and S. R. Elliott, *Europhys. Lett.* **39**, 37 (1997).
  - [7] G. Ruocco, F. Sette, R. Di Leonardo, G. Monaco, M. Sampoli, T. Scopigno, and G. Viliani, *Phys. Rev. Lett.* **84**, 5788 (2000).
  - [8] J. Horbach, W. Kob, and K. Binder, *Eur. Phys. J. B* **19**, 531 (2001).
  - [9] T. Scopigno, G. Ruocco, F. Sette, and G. Viliani, *Phys. Rev. E* **66**, 031205 (2002).
  - [10] O. Pilla, S. Caponi, A. Fontana, J. R. Gonçalves, M. Montagna, F. Rossi, G. Viliani, L. Angelani, G. Ruocco, G. Monaco, et al., *J. Phys.: Condens. Matter* **16**, 8519 (2004).
  - [11] B. Ruzicka, T. Scopigno, S. Caponi, A. Fontana, O. Pilla, P. Giura, G. Monaco, E. Pontecorvo, G. Ruocco, and F. Sette, *Phys. Rev. B* **69**, 100201(R) (2004).

- [12] T. Scopigno, U. Balucani, G. Ruocco, and F. Sette, Phys. Rev. Lett. **85**, 4076 (2000).
- [13] T. Scopigno, U. Balucani, G. Ruocco, and F. Sette, J. Phys. C **12**, 8009 (2000).
- [14] T. Scopigno, U. Balucani, G. Ruocco, and F. Sette, Phys. Rev. E **63**, 011210 (2000).
- [15] T. Scopigno, U. Balucani, G. Ruocco, and F. Sette, Phys. Rev. E **65**, 031205 (2002).
- [16] A. Monaco, T. Scopigno, P. Benassi, A. Giugni, G. Monaco, M. Nardone, G. Ruocco, and M. Sampoli, J. Chem. Phys. **120**, 8089 (2004).
- [17] T. Scopigno, E. Pontecorvo, R. Di Leonardo, M. Krisch, G. Monaco, G. Ruocco, B. Ruzicka, and F. Sette, J. Phys.: Condens. Matter **15**, S1269 (2003).
- [18] M. Sampoli, G. Ruocco, and F. Sette, Phys. Rev. Lett. **79**, 1678 (1997).
- [19] S. Sugai and A. Onodera, Phys. Rev. Lett. **77**, 4210 (1996).
- [20] Y. Inamura, M. Arai, N. Kitamura, S. M. Bennington, and A. C. Hannon, Physica B **241-243**, 903 (1998).
- [21] Y. Inamura, M. Arai, O. Yamamuro, A. Inaba, N. Kitamura, T. Otomo, T. Matsuo, S. M. Bennington, and A. C. Hannon, Physica B **263-264**, 299 (1999).
- [22] Y. Inamura, M. Arai, T. Otomo, N. Kitamura, and U. Buchenau, Physica B **284-288**, 1157 (2000).
- [23] W. Götze, in *Liquids, Freezing and Glass Transition*, edited by J.-P. Hansen, D. Levesque, and J. Zinn-Justin (North-Holland, Amsterdam, 1991), p. 287.
- [24] W. Götze and M. R. Mayr, Phys. Rev. E **61**, 587 (2000).
- [25] U. Bengtzelius, Phys. Rev. A **33**, 3433 (1986).
- [26] U. Bengtzelius, Phys. Rev. A **34**, 5059 (1986).
- [27] J.-P. Hansen and L. Verlet, Phys. Rev. **184**, 151 (1969).
- [28] U. Bengtzelius, W. Götze, and A. Sjölander, J. Phys. C **17**, 5915 (1984).
- [29] T. Franosch, M. Fuchs, W. Götze, M. R. Mayr, and A. P. Singh, Phys. Rev. E **55**, 7153 (1997).
- [30] M. Fuchs, W. Götze, and M. R. Mayr, Phys. Rev. E **58**, 3384 (1998).
- [31] W. Götze, J. Phys.: Condens. Matter **2**, 8485 (1990).
- [32] S.-H. Chong, W. Götze, and M. R. Mayr, Phys. Rev. E **64**, 011503 (2001).
- [33] The appearance of isothermal instead of adiabatic sound velocity is because energy fluctuations are not taken into account in the present study (*cf.* Ref. [5]).
- [34] For glass states, one obtains a slightly different expression than Eq. (22) when the generalized hydrodynamic approximation is applied to Eq. (14) instead of Eq. (12). As far as one is interested in the small- $q$  regime where  $\Omega_q$  can be approximated by its leading-order contribution,  $\Omega_q \approx qv_0$ , it does not matter whether the approximation is applied to Eq. (12) or (14), and this is the case in Sec. III where the  $q$  range of primary interest is  $q \lesssim 2$ . In Sec. IV, on the other hand, one needs to apply the approximation to Eq. (14) (*cf.* Eq. (34a)), since there we are also interested in larger  $q$  regime. The interested reader is referred to Ref. [24] for details.
- [35] W. Götze and L. Sjögren, J. Math. Analysis and Appl. **195**, 230 (1995).
- [36] Th. Voigtmann, J. Non-Cryst. Solids **307-310**, 188 (2002).
- [37] The formulas (31) can be applied only when  $w_1 \leq 1$  as discussed in Ref. [24]. We found, however, that  $w_1$  exceeds unity for  $\rho = 0.95$  and  $T = 0.5$ . Therefore, the SGA kernel  $\hat{m}_{\text{SGA}}(\omega)$  for this state has been obtained after solving the MCT equations (8d) and (9a) but dropping the two-mode contribution  $\hat{F}^{(2)}$  in the latter. As shown in Ref. [36], the difference between the SGA kernel so obtained and the one based on Eqs. (31) is small. The threshold frequencies  $\Omega_{\pm}$  for  $\rho = 0.95$  and  $T = 0.5$  have been determined as the frequencies where the intensity of  $\hat{m}_{\text{SGA}}(\omega)$  becomes 1% of its peak height.
- [38] C. Masciovecchio, G. Monaco, G. Ruocco, F. Sette, and M. Soltwisch, Philos. Mag. B **77**, 533 (1998).
- [39] G. Monaco, C. Masciovecchio, G. Ruocco, and F. Sette, Phys. Rev. Lett. **80**, 2161 (1998).
- [40] A. P. Sokolov, E. Rössler, A. Kisliuk, and D. Quitmann, Phys. Rev. Lett. **71**, 2062 (1993).
- [41] W. Götze and L. Sjögren, Z. Phys. B **65**, 415 (1987).
- [42] W. Götze and L. Sjögren, Rep. Prog. Phys. **55**, 241 (1992).
- [43] M. Fuchs, W. Götze, and A. Latz, Chem. Phys. **149**, 185 (1990).
- [44] G. Li, W. M. Du, J. Hernandez, and H. Z. Cummins, Phys. Rev. E **48**, 1192 (1993).